

Safe and Agile Transportation of Cable-Suspended Payload via Multiple Aerial Robots

Yongchao Wang^{*1}, Junjie Wang^{*2}, Xiaobin Zhou², Tiankai Yang², Chao Xu², and Fei Gao^{†2}

Abstract—Transporting a heavy payload using multiple aerial robots (MARs) is an efficient manner to extend the load capacity of a single aerial robot. However, existing schemes for the multiple aerial robots transportation system (MARTS) still lack the capability to generate a collision-free and dynamically feasible trajectory in real-time and further track an agile trajectory especially when there are no sensors available to measure the states of payload and cable. Therefore, they are limited to low-agility transportation in simple environments. To bridge the gap, we propose complete planning and control schemes for the MARTS, achieving safe and agile aerial transportation (SAAT) of a cable-suspended payload in complex environments. Flatness maps for the aerial robot considering the complete kinematical constraint and the dynamical coupling between each aerial robot and payload are derived. To improve the responsiveness for the generation of the safe, dynamically feasible, and agile trajectory in complex environments, a real-time spatio-temporal trajectory planning scheme is proposed for the MARTS. Besides, we break away from the reliance on the state measurement for both the payload and cable, as well as the closed-loop control for the payload, and propose a fully distributed control scheme to track the agile trajectory that is robust against imprecise payload mass and non-point mass payload. The proposed schemes are extensively validated through benchmark comparisons, ablation studies, and simulations. Finally, extensive real-world experiments are conducted on a MARTS integrated by three aerial robots with onboard computers and sensors. The result validates the efficiency and robustness of our proposed schemes for SAAT in complex environments.

Index Terms—Multiple Aerial Robots; Aerial Transportation; Trajectory Planning; Distributed Robust Control;

I. INTRODUCTION

AERIAL transportation is more time-efficient compared to ground transportation, as it is unaffected by terrain and traffic congestion. In areas such as logistics, medical rescue, and dangerous fire and disaster scenes, various time-sensitive supplies and equipment can be delivered by aerial transportation. Transporting a payload via just one aerial robot has been widely studied [1]–[9]. However, the limited load capacity of a single aerial robot greatly restricts its application in different fields.

Using MARs to transport a payload collaboratively can enhance the load capability of an aerial robot with arbitrary size. The payload can be attached to the MARs via rigid

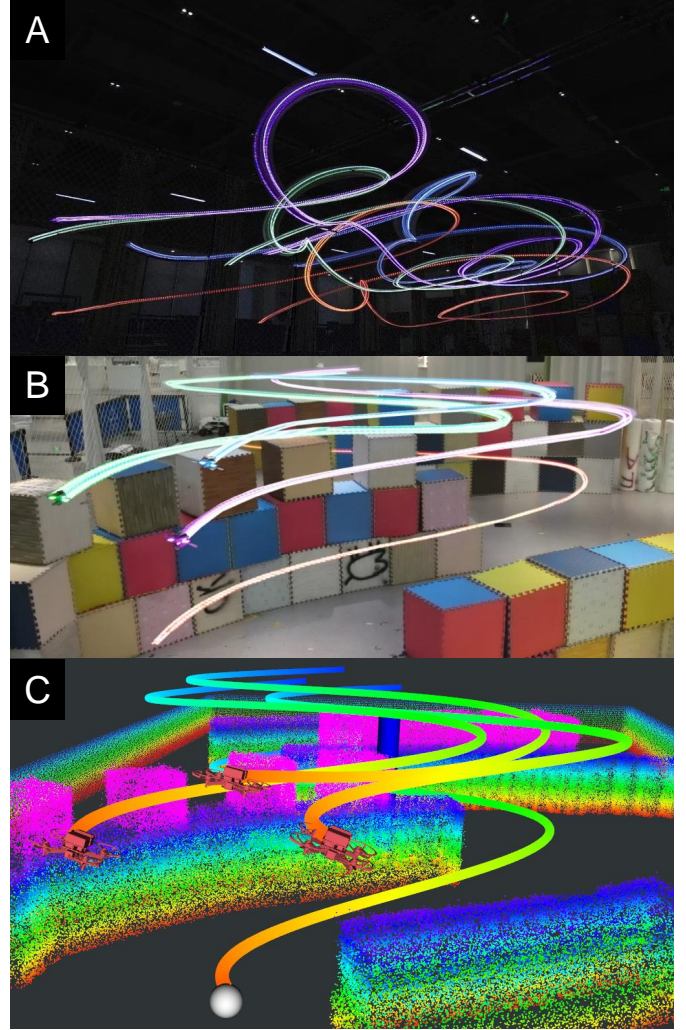


Fig. 1. Simulations and real-world experiments of our MARTS. (A) Agile transportation in free space, approaching the limit of thrust can be provided by the practical aerial robot in the MARTS. (B) and (C) display the actual snapshot and rviz simulation of the SAAT in a complex environment. Please watch our attached videos for more information at: <https://youtu.be/deD2wD673iI>.

connections such as grippers [10], electromagnets [11], and rigid rods [12], making up a large underactuated system whose acceleration can only be provided by first regulating the attitude of the whole system, thereby the agility reduces since the payload increases the system’s rotational inertia. Therefore, using cables to suspend the payload has attracted extensive interest from the robotics community [13]–[16] and is preferred as it not only eliminates the need for additional actuators and reduces structural complexity, thus increasing the load capacity of the system, but also allows agile transportation while minimizing the payload’s attitude. In this paper, we consider the cable-suspended payload transportation problem

^{*}Indicates equal contribution.

[†]Corresponding author: fgaoaa@zju.edu.cn.

¹School of Aeronautic Science and Engineering, Beihang University, Beijing 100191, China (e-mail: wangyongchao@buaa.edu.cn).

²Key Laboratory of Industrial Control Technology, Institute of Cyber-Systems and Control, Zhejiang University, Hangzhou 310027, China, and the Huzhou Institute, Zhejiang University, Huzhou 313000, China. (e-mail: www.wangjunjie@zju.edu.cn)

This work was supported by the National Natural Science Foundation of China under grant no. 62403419, and the Fundamental Research Funds for the Central Universities.

via the MARTS.

Speedy transportation of a payload in complex environments relies on a planner to generate a safe and agile trajectory, as well as a control scheme to track this trajectory. However, these are not easy works since the dynamical coupling and the kinematical constraint between each aerial robot and payload introduced by the tight cable complicate the problem. Several practical challenges are analyzed as follows.

The first challenge is how to ensure the *dynamical feasibility* of the agile trajectory planned for the MARTS with the dynamical coupling and the kinematical constraint. Due to the limited battery life, increasing the agility of trajectory is necessary to improve the mission efficiency [17]. However, as the trajectory becomes more agile, the state and control input of the aerial robot may transiently or persistently exceed the upper limits of its maneuvering capability, causing large tracking errors and thus resulting in system divergence and even crashes. Moreover, the dynamical coupling can exacerbate this trend. Therefore, flatness maps considering the dynamical coupling and the kinematical constraint existing in MARTS need to be derived to calculate the state and control input of each aerial robot, on which delicate constraints can be enforced to ensure the dynamical feasibility.

The second challenge is how to track an agile trajectory without state measurements of payload and cable even when there are uncertainties on the payload. Generally, a closed-loop control for the payload needs to be achieved in MARTS's control scheme. However, the controllers containing this closed-loop control are not suitable for the MARTS to track an agile trajectory. One reason is that the closed-loop control for the payload essentially acts as a centralized part of the MARTS's control scheme and the control law would be allocated and transmitted to each aerial robot, which not only induces disadvantageous time-delay but also inevitably propagates the oscillation in the control law to each aerial robot's desired position. Besides, from the mission perspective, it is not convenient to obtain precise priori information about the payload's mass. Moreover, it is not realistic to assemble sensors on the cables and especially the payload to measure their states, and the realistic payload cannot be strictly mass points. Therefore, a robust control scheme to uncertainties on the payload, getting rid of the reliance on the closed-loop control for payload as well as state measurements for both payload and cable, is necessary.

Apart from the above requirements, the safety of the trajectory and responsiveness of the planner must also be considered for the deployment of MARTS. Safety is crucial, as collisions involving the entire system with obstacles or reciprocal collisions between aerial robots can lead to crashes. Responsiveness is also important, as rapid trajectory generation enhances deployment speed and improves the system's ability to react to sudden changes, such as target alterations.

Based on the above analysis, we propose complete planning and control schemes for the MARTS. To the extent of our knowledge, this is the first work that achieves the real-time trajectory generation for SAAT of the cable-suspended payload by the MARTS in complex environments and achieves the transportation of a payload approaching the maximum agility

of the MARTS by pushing the aerial robot's thrust to its limit. In this work, we indirectly represent the aerial robot's position via the cable's directional vector and the payload's position, such that the kinematical constraint can be eliminated. Firstly, we derive the flatness maps considering the dynamical coupling and the kinematical constraint existing in MARTS to obtain the high-order states of the aerial robot. Secondly, we propose an efficient lightweight unconstrained trajectory planning scheme to fastly generate a trajectory based on a trajectory class represented by sparse spatio-temporal parameters. This planning scheme constructs not only the obstacle avoidance constraint for each component of MARTS and the reciprocal avoidance constraint for each pair of aerial robots to ensure safety, but also the delicate dynamical feasibility constraints to ensure the agile trajectory is dynamically executable. Besides, it also constructs vectorial constraints for each cable's force which are dexterously eliminated by diffeomorphisms to avoid the undesirable local-optimum trajectory. Thirdly, we propose a fully distributed control scheme to track the agile trajectory relying solely on the state measurements of aerial robots and is robust against the imprecise estimation of payload's mass and non-point mass payloads. Finally, we deploy our planning and control schemes on a practical MARTS consisting of three aerial robots and design various experiments to verify our schemes. Partial results are shown in Fig. 1. Contributions of this paper are listed as:

- 1) Flatness maps that consider the dynamical coupling and the kinematical constraint between each aerial robot and payload are derived based on the indirect position representation for the aerial robot.
- 2) A real-time trajectory planner for the MARTS, which considers the dynamical feasibility of aerial robots, the safety of the entire system in complex environments, and the finite vectorial ranges of cables, to generate safe and agile trajectories.
- 3) A robust and distributed control scheme to track the agile trajectory, which doesn't rely on the closed-loop control for payload and state measurements for both payload and cable and is robust against model uncertainties on the payload.
- 4) A variety of simulations and real-world experiments that validate the effectiveness of proposed planning and control schemes on a practical MARTS. Moreover, we open-source the code to facilitate further development of MARTS by the community.

II. RELATED WORKS

A. Motion Planning for MARTS

Several works [18]–[20] have investigated collaborative manipulation and transportation of a payload by MARTS based on the quasi-static assumption. However, these methods are severely limited because the inertial forces in agile transportation cannot be ignored simply.

Manubens et al. [21] use the Transition-based RRT to search for a collision-free non-smooth path for the MARTS. However, only simple dynamics are taken into account, so it is equally unsuitable for agile transportation. Sreenath et al. [22] reveal

that the MARTS is differentially flat when all the cables are tight and plan a smooth trajectory via minimizing the 6th derivative of flat output. However, the planning scheme neglects the safety of MARTS in complex environments and the dynamical feasibility of the planned trajectory. Besides, the deformation efficiency of the minimum-snap trajectory class [23], on which this scheme relies cannot guarantee the real-time performance of trajectory planning. Jackson et al. [24] consider the safety of MARTS in simple environments by simplifying the obstacle as a cylinder and the dynamical feasibility. They parallelize the solving of the optimization problem to mitigate the explosion of optimization time as the number of aerial robots increases. Nevertheless, it still takes a few seconds before the convergence even when the MARTS just consists of three aerial robots. Besides, the quality of the optimized trajectory is suspectable since they just enforce an incomplete kinematical constraint (relative distance constraint) between each aerial robot and payload and neglect the high-order constraints on relative velocity and acceleration. Sun et al. [25] consider the complete kinematical constraint and dynamical feasibility of trajectory and propose a real-time nonlinear model predictive control (NMPC) with high scalability to the number of aerial robots. However, they neglect the safety of MARTS in complex environments. Wahba et al. [26] consider not only the complete kinematical constraint but also the dynamical feasibility and the safety of MARTS in complex environments. However, they still do not address the real-time problem of trajectory planning.

B. Control for MARTS

Lee et al. [27], [28] propose geometric controllers for MARTS under an assumption that both the payload's state and the cable's state are known, considering the point-mass payload and the rigid body payload respectively. Li et al. [29] use monocular vision and inertial module to estimate the cable's state and partial payload's states in a distributed manner, but the payload's acceleration and jerk required to calculate the geometric control law are still neglected. All these controllers [27]–[29] cannot guarantee the avoidance of reciprocal collision between the aerial robots since they use a determinate minimum-norm principle to allocate each cable's desired force vector for payload's control. To ensure reciprocal avoidance, optimization-based [30] and NMPC-based [31] force allocation methods are proposed via exploiting the redundancy in the null space to ensure the minimum safe distance between the aerial robots. However, all the controllers [27]–[31] rely on special sensors or marks mounted on the payload to estimate or measure the payload's state, which is not convenient in practical deployment. Besides, the payload's acceleration and jerk, as well as the cable's angular rate introduce noise to the control law of the payload and lead to numerical instability. Moreover, all these controllers can be classified into centralized controllers for all the force allocations are centralized. The time-delay introduced by centralized computation and data transmission will limit the performances of these controllers, especially for agile transportation. Wahba et al. [32] propose a distributed force allocation method, in

which each aerial robot can update its desired force vector with a low frequency via optimizing the same problem existing only one global minima with the same input such that consistent results can be ensured. However, this method also does not fundamentally address the dependence on the payload's state and the detrimental effect of noise on control.

A common denominator of all the controllers [27]–[32] mentioned above is that they pursue the closed-loop control for payload. However, the oscillation existing in the payload's tracking error will directly lead to the oscillation of the aerial robot's desired position. Moreover, the control force for the payload can only be provided indirectly once the aerial robot has adjusted its attitude and the thrust to regulate the cable's force vector. Therefore, the response lag and the inevitable control error will fundamentally restrict the performance of these controllers. All these are the reasons why agile transportation is rarely seen in existing works.

To cope with the drawbacks of these controllers mentioned above, several fully distributed control schemes are proposed [33], [34]. They form a formation to transport the payload and simply treat the cable's force as an external disturbance that can be compensated via an observer. However, these control schemes neglect the negative influence induced by dynamical couplings. Besides, distributed lead-follower control schemes for the beam-like payload are studied in [35]–[37]. However, the follower's controller can only react to the leader's motion passively, which leads to a nonsmooth trajectory and is too short-sighted to avoid the reciprocal collision.

III. SYSTEM OVERVIEW AND PRELIMINARIES

A. System Architecture

The overall architecture of our planning and control schemes is illustrated in Fig. 2. Fusing LiDAR feature points with IMU data using FAST-lio2 [38] package, we construct the environmental map. A system-level global path planning method (Sec. V-A) that treats the MARTS as a convex and scalable orthopyramid is designed to find a global safe path based on this map, which acts as the initial value of the sparse parameters for the back-end safe and agile trajectory optimization.

For each iteration of the safe and agile trajectory optimization, the auxiliary sparse parameters ϖ^* , τ^* are firstly mapped to actual sparse parameters \mathbf{w} , \mathbf{T} , which is the unique representation for the trajectory, by diffeomorphisms (Sec. V-C1) such that the cable's vectorial constraints imposed on the actual sparse parameters can be eliminated directly. Then, a new trajectory can be generated from the actual sparse parameters by calculating a system of linear equations with linear spatio-temporal computational complexity (Sec. IV-B). Next, we calculate the high-order states and control input using the flatness maps (Sec. IV-A) such that the quality of trajectory can be evaluated in terms of the safety (Sec. IV-C), the dynamical feasibility (Sec. IV-D) and the coupled dynamical constraint (Sec. IV-E) specifically existing in our scheme. Besides, the total penalty cost and the gradients w.r.t the trajectory's parameters \mathbf{c} , \mathbf{T} are computed consequently. Finally, these gradients are backpropagated in turn to the gradients w.r.t

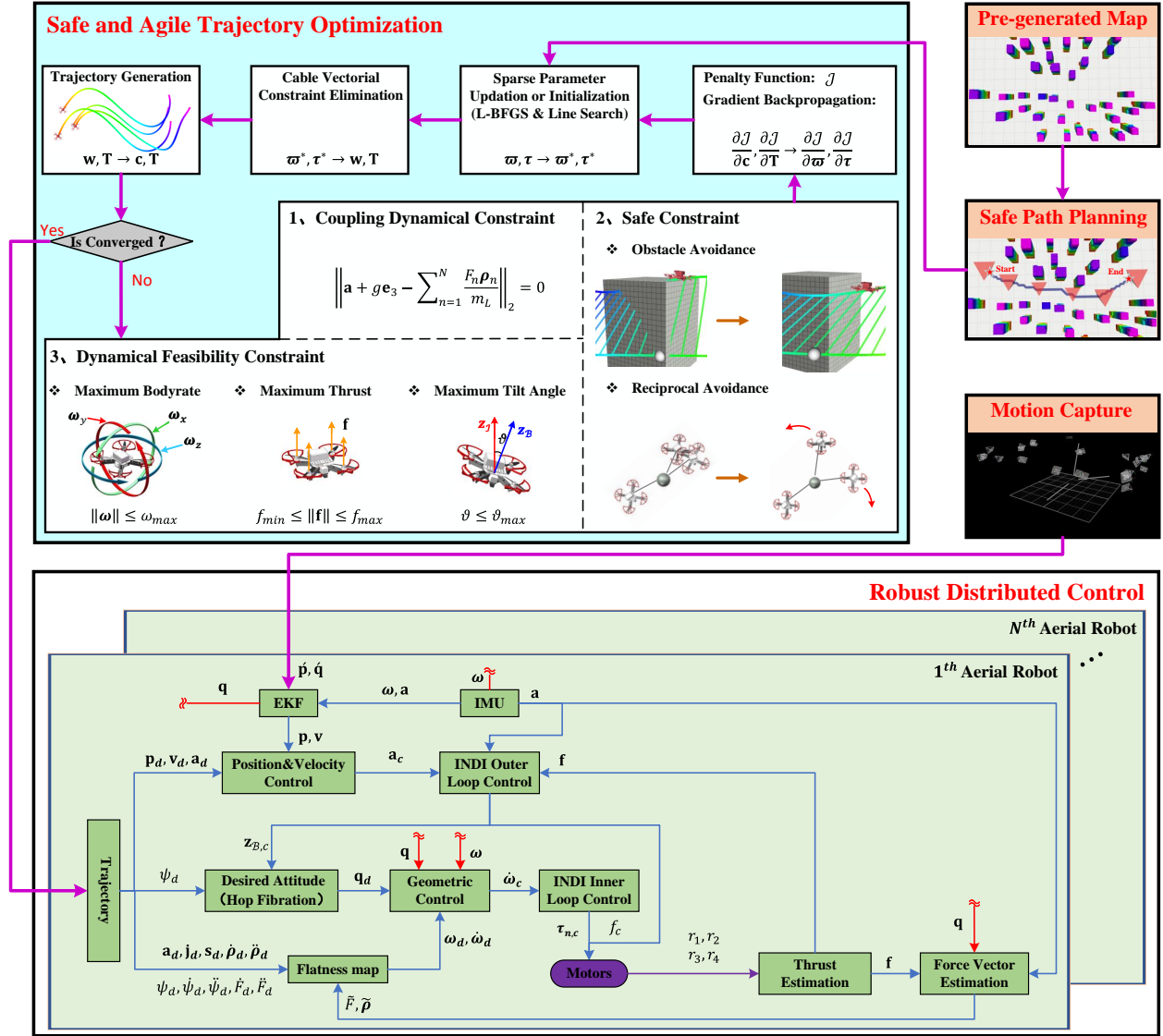


Fig. 2. An overview of our safe and agile trajectory planning scheme and robust distributed control scheme for MARTS.

the actual and auxiliary sparse parameters consequently, based on which the auxiliary sparse parameters update to new values (Sec. V-D). The optimized trajectory will be transmitted to each aerial robot when the optimization satisfies the condition of convergence.

We get the odometry for each aerial robot using an extended Kalman filter (EKF) to fuse the position and velocity from the motion capture system with the onboard IMU data. Our robust and distributed control scheme mainly includes a two-loop control method shared by all the aerial robots. The motor's revolutions per minute (RPM) are measured to estimate the thrust and control torque of the aerial robot. The outer loop (Sec. VI-A) adopts the incremental nonlinear dynamic inversion (INDI) [39] to get the thrust vector command based on the closed-loop trajectory tracking control law, the filter acceleration, and the estimated thrust vector. The inner loop (Sec. VI-B) adopts the hop fibration rotation factorization to reconstruct the desired attitude and calculate the desired body rate as well as angular acceleration by flatness maps, which

also uses INDI to get the control torque command based on the geometric attitude control law, the estimated angular acceleration, and the estimated control torque. Finally, the control commands are transformed into the signals to control each motor's RPM.

B. Dynamics Model

In this paper, we consider a point-mass payload transported by a MARTS consisting of N aerial robots, as is illustrated in Fig 3. Necessary symbols to describe the dynamics model are defined in the Tab. I. The payload is suspended on each aerial robot by a massless cable. It should be pointed out that frequent transitions of the cable between slack mode and taut mode will lead to switching of dynamics model, which is detrimental to control and can even cause dangerous system collapse. To address this risk, our planner will avoid the slack mode and generate a trajectory that always maintains the taut mode. Therefore, we only need to consider the following

TABLE I
SYMBOL DEFINITION

Symbol	Definition
$\mathcal{I}, \mathcal{B}_n$	world frame, the n^{th} robot's body frame
$\mathbf{z}_{\mathcal{I}}, \mathbf{z}_{\mathcal{B}_n}^n \in \mathbb{R}^3$	z -axes of \mathcal{I} and \mathcal{B}_n
\mathbf{e}_3	unit vector $[0, 0, 1]^T$
$m_L \in \mathbb{R}_{>0}$	mass of payload
$m_n \in \mathbb{R}_{>0}$	mass of the n^{th} aerial robot
$\mathbf{J}_n \in \mathbb{R}^{3 \times 3}$	rotational inertia of the n^{th} aerial robot
$\mathbf{p}, \mathbf{v} \in \mathbb{R}^3$	position and velocity of payload
$\mathbf{p}_n, \mathbf{v}_n \in \mathbb{R}^3$	position and velocity of the n^{th} aerial robot
$\mathbf{p}_n^k \in \mathbb{R}^3$	position of the k^{th} sampled point on the n^{th} cable
$\mathbf{R}_n \in \text{SO}(3)$	rotation matrix of the n^{th} aerial robot
$\psi_n \in \mathbb{R}$	yaw angle of the n^{th} aerial robot
$\vartheta_n \in \mathbb{R}$	tilt angle of the n^{th} aerial robot, i.e., the angle between $\mathbf{z}_{\mathcal{B}_n}^n$ and $\mathbf{z}_{\mathcal{I}}$
\mathbf{q}_n	quaternion of the n^{th} aerial robot
$\boldsymbol{\omega}_n \in \mathbb{R}^3$	body rate w.r.t \mathcal{B}_n of the n^{th} aerial robot
$\boldsymbol{\rho}_n \in S^2$	unit vector of the n^{th} cable w.r.t \mathcal{I} , pointing from payload to the n^{th} aerial robot
$\boldsymbol{\tau}_n \in \mathbb{R}^3$	control moment of the n^{th} aerial robot w.r.t \mathcal{B}_n
$\mathbf{f}_n \in \mathbb{R}^3$	mass-normalized thrust vector of the n^{th} aerial robot
$f_n \in \mathbb{R}_{>0}$	mass-normalized thrust of the n^{th} aerial robot
$F_n \in \mathbb{R}_{>0}$	tension of the n^{th} cable
$\theta_n, \phi_n \in \mathbb{R}$	pitch angle, azimuth angle of the n^{th} cable w.r.t \mathcal{I}
$l \in \mathbb{R}_{>0}$	length of the n^{th} cable
$g \in \mathbb{R}_{>0}$	gravitational acceleration

consistent dynamical model for the taut mode. The dynamics model of the payload is written as

$$\dot{\mathbf{p}} = \mathbf{v}, \quad (1a)$$

$$\dot{\mathbf{v}} = -g\mathbf{e}_3 + \sum_{n=1}^N F_n \boldsymbol{\rho}_n / m_L. \quad (1b)$$

Besides, all the aerial robots share the same dynamics model and the dynamics model of the n^{th} aerial robot is written as

$$\dot{\mathbf{p}}_n = \mathbf{v}_n, \quad (2a)$$

$$\dot{\mathbf{v}}_n = -g\mathbf{e}_3 + f_n \mathbf{R}_n \mathbf{e}_3 / m_n - F_n \boldsymbol{\rho}_n / m_n, \quad (2b)$$

$$\dot{\mathbf{R}}_n = \mathbf{R}_n \hat{\boldsymbol{\omega}}_n, \quad (2c)$$

$$\mathbf{J}_n \dot{\boldsymbol{\omega}}_n = -\boldsymbol{\omega}_n \times \mathbf{J}_n \boldsymbol{\omega}_n + \boldsymbol{\tau}_n, \quad (2d)$$

where $\hat{\cdot}$ is the operator to get the skew-symmetric matrix.

C. Kinematic Constraint Elimination

The n^{th} taut cable imposes a kinematic constraint between the payload and the n^{th} aerial robot

$$\|\mathbf{p}_n - \mathbf{p}\|_2 \equiv l. \quad (3)$$

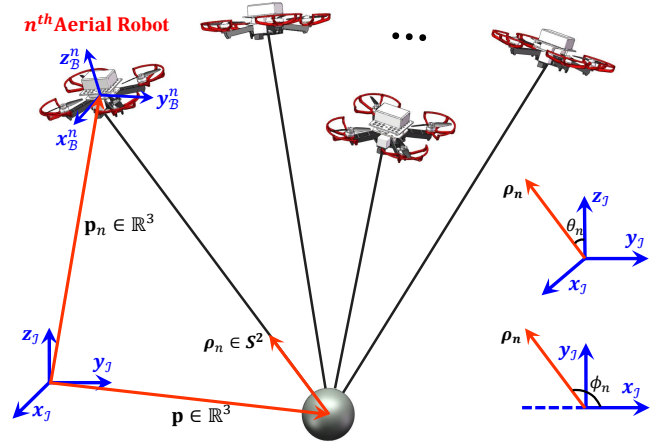


Fig. 3. Illustration of the cable-suspended payload transportation by the MARTS and the definition of θ_n, ϕ_n used to represent $\boldsymbol{\rho}_n$.

It should be pointed out that the differentials of Eq. 3 also implicitly enforce constraints on \mathbf{v}_n, \mathbf{v} and their high-order derivatives. In this paper, we use payload's position \mathbf{p} and n^{th} cable's direction vector $\boldsymbol{\rho}_n$ to indirectly represent the n^{th} aerial robot's position

$$\mathbf{p}_n = \mathbf{p} + l\boldsymbol{\rho}_n, \quad (4)$$

such that \mathbf{p}, \mathbf{p}_n , as well as their high-order derivatives always satisfy the complete kinematic constraint enforced by Eq. 3, which is eliminated subsequently.

In general, as in work [22], the three components of force vector $F_n \boldsymbol{\rho}_n$ can be chosen as the variables to represent $F_n \boldsymbol{\rho}_n$. Thus, through unitizing $F_n \boldsymbol{\rho}_n$, $\boldsymbol{\rho}_n$ can be got to solve \mathbf{p}_n . However, when the norm $\|F_n \boldsymbol{\rho}_n\|_2$ converges to zero, there exists a singularity problem in solving \mathbf{p}_n . To avoid this singularity, we introduce two variables, i.e., the pitch angle θ_n and the azimuth angle ϕ_n of the n^{th} cable as depicted in Fig. 3. Thus, $\boldsymbol{\rho}_n$ can be represented as

$$\boldsymbol{\rho}_n = [\cos(\theta_n) \cos(\phi_n), \cos(\theta_n) \sin(\phi_n), \sin(\theta_n)]^T. \quad (5)$$

Let $\boldsymbol{\xi}_n = (\theta_n, \phi_n, F_n)^T \in \mathbb{R}^3$, thus $F_n \boldsymbol{\rho}_n$ can be uniquely represented by $\boldsymbol{\xi}_n$. Using $\boldsymbol{\xi}_n$ as the variable also brings an advantage that the constraints related to the direction and magnitude of $F_n \boldsymbol{\rho}_n$ can be enforced on $\boldsymbol{\xi}_n$ directly without constructing nonlinear maps to calculate $\boldsymbol{\xi}_n$ from $F_n \boldsymbol{\rho}_n$ such that these constraints can be eliminated via designing a diffeomorphism conveniently (Sec. V-C1).

D. Extended Flat-output Variable

The MARTS is a differential flatness system. For the n^{th} aerial robot, $\mathbf{p}, \boldsymbol{\xi}_n$, and ψ_n act as the flat-output variable. Compositing \mathbf{p} and $\boldsymbol{\xi}_n, \psi_n$ for all $n \in [1, \dots, N]$ yields a variable

$$\mathbf{Z} = (\mathbf{p}^T, \boldsymbol{\xi}_1^T, \psi_1, \dots, \boldsymbol{\xi}_N^T, \psi_N)^T \in \mathbb{R}^{4N+3}, \quad (6)$$

called as the extended flat-output variable for MARTS. Actually, $\mathbf{Z} \setminus \{\boldsymbol{\xi}_N\} \in \mathbb{R}^{4N}$ can act as one selection of flat-output variable for MARTS since $\mathbf{Z} \setminus \{\boldsymbol{\xi}_N\}$ is sufficient to uniformly

determine ξ_N as elaborated in [22]. To avoid the complex map from $\mathbf{Z} \setminus \{\xi_N\}$ onto ξ_N , we relieve ξ_N 's binding on $\mathbf{Z} \setminus \{\xi_N\}$ and append redundant degree of freedom (DoF) ξ_N into \mathbf{Z} . As a result, we need to enforce a supererogatory dynamical constraint (Eq. 1b) onto \mathbf{Z} during the optimization (Sec. IV-E). The differential flatness characteristics help us to optimize a trajectory just on the low-dimensional extended flat-output space \mathbf{Z} .

For any $s \in \{s | s \in \mathbb{N}_+, s \geq 1\}$, we denote $\mathbf{Z}^{[s-1]} \in \mathbb{R}^{s \times (4N+3)}$ as

$$\mathbf{Z}^{[s-1]} = (\mathbf{Z}^T, \dot{\mathbf{Z}}^T, \dots, \mathbf{Z}^{(s-1)T})^T. \quad (7)$$

IV. PLANNING FOR SAFE AND AGILE TRANSPORTATION

A. Flatness Maps

In this section, we derive the flatness maps for the n^{th} aerial robot based on the indirect representation (Eq. 4). Firstly, from (Eq. 2b), we can get its mass-normalized thrust vector

$$\mathbf{f}_n = \ddot{\mathbf{p}} + l\ddot{\boldsymbol{\rho}}_n + g\mathbf{e}_3 + F_n\boldsymbol{\rho}_n/m. \quad (8)$$

Since the direction of \mathbf{f}_n is parallel to \mathbf{z}_B^n , we can obtain

$$\mathbf{z}_B^n = \mathcal{N}(\mathbf{f}_n), \quad (9)$$

where $\mathcal{N}() : \mathbb{R}^3 \rightarrow \mathbb{R}^3$ is the vector unitization function defined as $\mathcal{N}(\mathbf{x}) \triangleq \mathbf{x}/\|\mathbf{x}\|_2, \mathbf{x} \in \mathbb{R}^3$. To recover the quaternion \mathbf{q}_n w.r.t \mathbf{R}_n from \mathbf{z}_B^n, ψ_n , we use the rotation factorization known as Hopf Fibration [40], which introduces the fewest singularities. The body frame \mathbf{z}_B^n is constructed through rotating the world frame \mathcal{I} around its z-axis $\mathbf{z}_{\mathcal{I}}$ by ψ_n and continually rotating it around the current y-axis till its z-axis coincides with \mathbf{z}_B^n , whose quaternion \mathbf{q}_n can be computed as

$$\mathbf{q}_n = \mathbf{q}_{z_B^n} \odot \mathbf{q}_{\psi_n}, \quad (10)$$

where \odot is the quaternion multiplication. For arbitrary vector $\mathbf{x} \in \mathbb{R}^3$ and quaternion \mathbf{q} , let $\mathbf{x}_1, \mathbf{x}_2, \mathbf{x}_3$ denote the three elements of \mathbf{x} , and let $\mathbf{q}^w, \mathbf{q}^x, \mathbf{q}^y, \mathbf{q}^z$ denote the four elements of \mathbf{q} . Thus, $\mathbf{q}_{\psi_n}^i, \mathbf{q}_{z_B^n}^i$ can be expanded as

$$\mathbf{q}_{\psi_n} = \left(\cos \frac{\psi_n}{2}, 0, 0, \sin \frac{\psi_n}{2} \right), \quad (11a)$$

$$\mathbf{q}_{z_B^n} = \frac{1}{\sqrt{2(\mathbf{z}_{B,3}^n + 1)}} (\mathbf{z}_{B,3}^n + 1, -\mathbf{z}_{B,2}^n, \mathbf{z}_{B,1}^n, 0). \quad (11b)$$

Since the tilt angle ϑ_n is only related to $\mathbf{q}_n^x, \mathbf{q}_n^y$, we just give the formulation of $\mathbf{q}_n^x, \mathbf{q}_n^y$ as follows,

$$\mathbf{q}_n^x = \frac{-1}{\sqrt{2(\mathbf{z}_{B,3}^n + 1)}} \left(\mathbf{z}_{B,2}^n \cos \frac{\psi_n}{2} - \mathbf{z}_{B,1}^n \sin \frac{\psi_n}{2} \right), \quad (12a)$$

$$\mathbf{q}_n^y = \frac{1}{\sqrt{2(\mathbf{z}_{B,3}^n + 1)}} \left(\mathbf{z}_{B,1}^n \cos \frac{\psi_n}{2} + \mathbf{z}_{B,2}^n \sin \frac{\psi_n}{2} \right). \quad (12b)$$

Now, the tilt angle ϑ_n can be calculated by

$$\vartheta_n = \text{acos} \left[1 - 2 \left(\mathbf{q}_n^{x2} + \mathbf{q}_n^{y2} \right) \right], \quad (13)$$

and the body rate $\boldsymbol{\omega}_n$ can be calculated by

$$\boldsymbol{\omega}_n = 2\mathbf{q}_n^{-1} \odot \dot{\mathbf{q}}_n. \quad (14)$$

Finally, inverting and differentiating \mathbf{q}_n gives

$$\boldsymbol{\omega}_{n,1} = \dot{\mathbf{z}}_{B,1}^n \sin(\psi_n) - \dot{\mathbf{z}}_{B,2}^n \cos(\psi_n) - \frac{\dot{\mathbf{z}}_{B,3}^n [\mathbf{z}_{B,1}^n \sin(\psi_n) - \mathbf{z}_{B,2}^n \cos(\psi_n)]}{\mathbf{z}_{B,3}^n + 1}, \quad (15a)$$

$$\boldsymbol{\omega}_{n,2} = \dot{\mathbf{z}}_{B,1}^n \cos(\psi_n) + \dot{\mathbf{z}}_{B,2}^n \sin(\psi_n) - \frac{\dot{\mathbf{z}}_{B,3}^n [\mathbf{z}_{B,1}^n \cos(\psi_n) + \mathbf{z}_{B,2}^n \sin(\psi_n)]}{\mathbf{z}_{B,3}^n + 1}, \quad (15b)$$

$$\boldsymbol{\omega}_{n,3} = \frac{\mathbf{z}_{B,2}^n \dot{\mathbf{z}}_{B,1}^n - \mathbf{z}_{B,1}^n \dot{\mathbf{z}}_{B,2}^n}{\mathbf{z}_{B,3}^n + 1} + \dot{\psi}_n, \quad (15c)$$

where $\dot{\mathbf{z}}_B^n$ is the vector differentiation derived as

$$\dot{\mathbf{z}}_B^n = \frac{1}{\|\mathbf{f}_n\|_2} \left(\mathbf{I} - \frac{\mathbf{f}_n \mathbf{f}_n^T}{\|\mathbf{f}_n\|_2^2} \right) \dot{\mathbf{f}}_n, \quad (16a)$$

$$\dot{\mathbf{f}}_n = \ddot{\mathbf{p}} + l\ddot{\boldsymbol{\rho}}_n + \frac{1}{m} (\dot{F}_n \boldsymbol{\rho}_n + F_n \dot{\boldsymbol{\rho}}_n). \quad (16b)$$

B. Trajectory Representation

Flatness maps rely only on the flat-output variable, which avoid integrating the dynamical equations to obtain the state and the control input. In this paper, we use a multidimensional piecewise polynomial to represent the flat-output trajectory so that the motion planning for MARTS can be performed by the deformation of the flat-output trajectory. Let $\mathbf{Z}(t)$ denote a $(4N+3)$ -dimension, M -piece polynomial of $2s$ -order. The m^{th} piece of $\mathbf{Z}(t)$ is defined as

$$\mathbf{Z}|_m(t) = \mathbf{c}_m^T \boldsymbol{\beta}(t), \quad \forall t \in [0, T_m], \quad (17)$$

where $\mathbf{c}_m \in \mathbb{R}^{2s \times (4N+3)}$ is the coefficient matrix, $\boldsymbol{\beta}(t) = [1, t^1, \dots, t^{2s-1}]^T$ is the natural basis and $T_m \in \mathbb{R}_{>0}$ is the time duration of the m^{th} piece. Thus, the flat-output trajectory $\mathbf{Z}(t)$ can be fully represented by the coefficient matrix $\mathbf{c} = (\mathbf{c}_1^T, \dots, \mathbf{c}_M^T)^T \in \mathbb{R}^{2sM \times (4N+3)}$ and the time vector $\mathbf{T} = (T_1, \dots, T_M)^T \in \mathbb{R}_{>0}^M$.

To improve the efficiency of trajectory optimization, we adopt $\mathcal{C}_{\text{MINCO}}$ [41], a state-of-the-art (SOTA) polynomial trajectory class. Given a set of sparse representation parameters $\{\mathbf{w}, \mathbf{T}\}$, $\mathcal{C}_{\text{MINCO}}$ constructs a system of linear equations \mathcal{L} to solve $\{\mathbf{c}, \mathbf{T}\}$ from $\{\mathbf{w}, \mathbf{T}\}$

$$(\mathbf{c}, \mathbf{T}) = \mathcal{L}(\mathbf{w}, \mathbf{T}), \quad (18)$$

such that a piecewise polynomial, i.e., the flat-output trajectory $\mathbf{Z}(t)$ is generated, where $\mathbf{w} = (\mathbf{w}_1, \dots, \mathbf{w}_{M-1})^T \in \mathbb{R}^{(4N+3) \times (M-1)}$ and for any $m' \in [1, \dots, M-1]^T$, $\mathbf{w}_{m'} = (\mathbf{p}^{m'T}, \boldsymbol{\xi}_1^{m'T}, \psi_1^{m'}, \dots, \boldsymbol{\xi}_N^{m'T}, \psi_N^{m'})^T \in \mathbb{R}^{4N+3}$ is the m'^{th} junction to connect the m'^{th} piece and the $(m'+1)^{\text{th}}$ piece. Using $\{\mathbf{w}, \mathbf{T}\}$ to determine the continuity conditions at the junctions, with the boundary conditions at the initial and final moments, $\mathcal{C}_{\text{MINCO}}$ can uniquely generate a minimum control effort trajectory that satisfies all these conditions by solving \mathcal{L} directly, while avoiding time-consuming iterative optimization.

C. Safety Constraints

The collapse of MARTS occurs when any part of the system collides with the obstacles in a complex environment, or when

any two aerial robots within the system reciprocally collide with each other. In this section, we construct safety constraints to avoid obstacle collisions and reciprocal collisions between the aerial robots. Besides, we also design the differential metrics and derive corresponding gradients w.r.t trajectory's parameter, i.e., \mathbf{c} , \mathbf{T} . In the following sections, we assume that all the states and control input defined in Tab. I are associated with a special point on the m^{th} piece of trajectory. The details are given as follows.

1) *Obstacle Avoidance Constraint*: The obstacle avoidance constraint is designed to avoid obstacle collisions. Complete obstacle avoidance means that the N surfaces swept by all cables' trajectories, the N aerial robots' trajectories, and the payload's trajectory should not be intersected by any obstacle. In this work, we maintain an Euclidean Signed Distance Field (ESDF). To evaluate the safety margin between a point $\mathbf{p}^* \in \mathbb{R}^3$ and the obstacle, we design a differential metric $\mathcal{M}_{oa} : \mathbb{R}^3 \times \mathbb{R}_{>0} \rightarrow \mathbb{R}$ as

$$\mathcal{M}_{oa}(\mathbf{p}^*, d) = d - \mathcal{E}(\mathbf{p}^*), \quad (19)$$

where $\mathcal{E}(\mathbf{p}^*)$ is the distance between \mathbf{p}^* and its closest obstacle evaluated by ESDF and $d \in \mathbb{R}_{>0}$ is the safety distance away from obstacle.

Let $d_{oa}^c \in \mathbb{R}_{>0}$, $d_{oa}^Q \in \mathbb{R}_{>0}$, $d_{oa}^L \in \mathbb{R}_{>0}$ denote the safe distances of the cable's sampled point, the aerial robot, and the payload respectively. We enforce the obstacle avoidance constraint on the payload

$$\mathcal{M}_{oa}(\mathbf{p}, d_{oa}^L) < 0. \quad (20)$$

For any $n \in [1, \dots, N]$, we enforce obstacle avoidance constraint on the n^{th} aerial robot

$$\mathcal{M}_{oa}(\mathbf{p}_n, d_{oa}^Q) < 0. \quad (21)$$

For the n^{th} cable, we uniformly sample K points along the cable. For each $k \in [1, \dots, K]$ and each $n \in [1, \dots, N]$, we enforce the obstacle avoidance constraint on the k^{th} sampled points \mathbf{p}_n^k along the n^{th} cable

$$\mathcal{M}_{oa}(\mathbf{p}_n^k, d_{oa}^c) < 0, \quad (22)$$

where \mathbf{p}_n^k can be computed as

$$\mathbf{p}_n^k = \mathbf{p} + \frac{lk}{K+1} \boldsymbol{\rho}_n. \quad (23)$$

Then the penalty function \mathcal{J}_{oa}^0 for the constraint enforced on the payload in Eq. 20 is defined as

$$\mathcal{J}_{oa}^0 = \mathcal{L}_\mu [\mathcal{M}_{oa}(\mathbf{p}, d_{oa}^L)], \quad (24)$$

Besides, the penalty function \mathcal{J}_{oa}^n for the constraints w.r.t both the n^{th} aerial robot and n^{th} cable in Eq. 21 - Eq. 22 is defined as

$$\mathcal{J}_{oa}^n = \sum_{k=1}^K \mathcal{L}_\mu [\mathcal{M}_{oa}(\mathbf{p}_n^k, d_{oa}^c)] + \mathcal{L}_\mu [\mathcal{M}_{oa}(\mathbf{p}_n, d_{oa}^Q)], \quad (25)$$

where $\mathcal{L}_\mu : \mathbb{R} \rightarrow \mathbb{R}$ is a C^2 -smoothing function defined as

$$\mathcal{L}_\mu(x) = \begin{cases} 0, & x \leq 0, \\ (\mu - x/2)(x/\mu)^3, & 0 < x \leq \mu, \\ x - \mu/2, & x > \mu, \end{cases} \quad (26)$$

which smooths the transition of a truncated linear function at $x = 0$.

Finally, the gradients of $\mathcal{M}_{oa}(\mathbf{p}, d_{oa}^L)$ w.r.t \mathbf{c}_m, T_m are derived as

$$\frac{\partial \mathcal{M}_{oa}(\mathbf{p}, d_{oa}^L)}{\partial \mathbf{c}_{m,\mathbf{p}}} = -\nabla \mathcal{E}(\mathbf{p})^T \otimes \boldsymbol{\beta}, \quad (27a)$$

$$\frac{\partial \mathcal{M}_{oa}(\mathbf{p}, d_{oa}^L)}{\partial T_m} = -\nabla \mathcal{E}(\mathbf{p})^T \mathbf{v}, \quad (27b)$$

where \otimes is the Kronecker product and $\nabla \mathcal{E} : \mathbb{R}^3 \rightarrow \mathbb{R}^3$ is an operator to query the ESDF gradient.

Let $\boldsymbol{\Phi}_n$ denotes $(\theta_n, \phi_n)^T$ and $\varrho_k = lk/(K+1)$. The gradients of $\mathcal{M}_{oa}(\mathbf{p}_n^k, d_{oa}^c)$ w.r.t \mathbf{c}_m, T_m are computed as

$$\frac{\partial \mathcal{M}_{oa}(\mathbf{p}_n^k, d_{oa}^c)}{\partial \mathbf{c}_{m,\mathbf{p}}} = -\nabla \mathcal{E}(\mathbf{p}_n^k)^T \otimes \boldsymbol{\beta}, \quad (28a)$$

$$\frac{\partial \mathcal{M}_{oa}(\mathbf{p}_n^k, d_{oa}^c)}{\partial \mathbf{c}_{m,\boldsymbol{\Phi}_n}} = -\varrho_k \left(\nabla \mathcal{E}(\mathbf{p}_n^k)^T \frac{\partial \boldsymbol{\rho}_n}{\partial \boldsymbol{\Phi}_n} \right) \otimes \boldsymbol{\beta}, \quad (28b)$$

$$\frac{\partial \mathcal{M}_{oa}(\mathbf{p}_n^k, d_{oa}^c)}{\partial \mathbf{c}_{m,F_n}} = \mathbf{0}, \quad (28c)$$

$$\frac{\partial \mathcal{M}_{oa}(\mathbf{p}_n^k, d_{oa}^c)}{\partial T_m} = -\left(\dot{\mathbf{p}} + \varrho_k \frac{\partial \boldsymbol{\rho}_n}{\partial \boldsymbol{\Phi}_n} \dot{\boldsymbol{\Phi}}_n \right)^T \nabla \mathcal{E}(\mathbf{p}_n^k). \quad (28d)$$

Note that $\mathbf{c}_{m,\mathbf{p}}$ denotes the submatrix of \mathbf{c}_m w.r.t the variable \mathbf{p} in \mathbf{Z} . The gradients of $\mathcal{M}_{oa}(\mathbf{p}_n, d_{oa}^Q)$ w.r.t \mathbf{c}_m, T_m can be computed similarly as in Eq. 28a - Eq. 28d except that the \mathbf{p}_n^k, d_{oa}^c , and ϱ_k are need to be substituted by \mathbf{p}_n, d_{oa}^Q , and 1, which are omitted here.

2) *Reciprocal Avoidance Constraint*: The reciprocal avoidance constraint is designed to avoid reciprocal collisions among the aerial robots. To evaluate the safety margin between two aerial robots, we design a differential metric $\mathcal{M}_{ra} : \mathbb{R}^3 \times \mathbb{R}^3 \times \mathbb{R}_{>0} \rightarrow \mathbb{R}$ as

$$\mathcal{M}_{ra}(\mathbf{p}, \mathbf{p}', d) = d^2 - \|\mathbf{p} - \mathbf{p}'\|^2, \quad (29)$$

For each $n \in [1, \dots, N-1]$ and each $n' \in [n+1, \dots, N]$, we enforce the reciprocal avoidance constraint between the n^{th} aerial robot and the n'^{th} aerial robot

$$\mathcal{M}_{ra}(\mathbf{p}_n, \mathbf{p}_{n'}, d_{ra}^Q) < 0, \quad (30a)$$

where $d_{ra}^Q \in \mathbb{R}_{>0}$ is the safe distance between the aerial robots. Then, the penalty function \mathcal{J}_{ra} for all the reciprocal avoidance constraints is defined as

$$\mathcal{J}_{ra} = \sum_{i=1}^{N-1} \sum_{j=i+1}^N \mathcal{L}_\mu [\mathcal{M}_{ra}(\mathbf{p}_i, \mathbf{p}_j, d_{ra}^Q)]. \quad (31)$$

Finally, the gradients of $\mathcal{M}_{ra}(\mathbf{p}_i, \mathbf{p}_j, d_{ra}^Q)$ w.r.t \mathbf{c}_m, T_m are computed as

$$\frac{\partial \mathcal{M}_{ra}(\mathbf{p}_i, \mathbf{p}_j, d_{ra}^Q)}{\partial \mathbf{c}_{m,\mathbf{p}}} = \mathbf{0}, \quad (32a)$$

$$\frac{\partial \mathcal{M}_{ra}(\mathbf{p}_i, \mathbf{p}_j, d_{ra}^Q)}{\partial \mathbf{c}_{m,\mathbf{p}_i}} = -2l \left[(\mathbf{p}_i - \mathbf{p}_j)^T \frac{\partial \boldsymbol{\rho}_i}{\partial \boldsymbol{\Phi}_i} \right] \otimes \boldsymbol{\beta}, \quad (32b)$$

$$\frac{\partial \mathcal{M}_{ra}(\mathbf{p}_i, \mathbf{p}_j, d_{ra}^Q)}{\partial \mathbf{c}_{m,\mathbf{p}_j}} = 2l \left[(\mathbf{p}_i - \mathbf{p}_j)^T \frac{\partial \boldsymbol{\rho}_j}{\partial \boldsymbol{\Phi}_j} \right] \otimes \boldsymbol{\beta}, \quad (32c)$$

$$\frac{\partial \mathcal{M}_{ra}(\mathbf{p}_i, \mathbf{p}_j, d_{ra}^Q)}{\partial \mathbf{c}_{m, F_i}} = \frac{\partial \mathcal{M}_{ra}(\mathbf{p}_i, \mathbf{p}_j, d_{ra}^Q)}{\partial \mathbf{c}_{m, F_j}} = \mathbf{0}, \quad (32d)$$

$$\frac{\partial \mathcal{M}_{ra}(\mathbf{p}_i, \mathbf{p}_j, d_{ra}^Q)}{\partial T_m} = -2l \left(\frac{\partial \rho_i}{\partial \Phi_i} \dot{\Phi}_i - \frac{\partial \rho_j}{\partial \Phi_j} \dot{\Phi}_j \right)^T \cdot (\mathbf{p}_i - \mathbf{p}_j). \quad (32e)$$

D. Dynamical Feasibility Constraints

For any aerial robot in the MARTS, an overrun of either its state or control input will cause the MARTS to crash. In this section, we enforce dynamical feasibility constraints on the state and control input of each aerial robot to ensure that an agile trajectory can be executed by the practical MARTS. These constraints are designed to limit transient state and control input along the trajectory when the agility enhances as the trajectory's duration decreases, which involve four types for each aerial robot, i.e., a constraint on maximum velocity, a constraint on maximum and minimum mass-normalized thrust, a constraint on maximum tilt angle, and a constraint on maximum body rate. The details are given as follows.

1) *Maximum Velocity Constraint:* For a scalar a , we define a metric $\mathcal{M} : \mathbb{R} \times \mathbb{R}_{>0} \rightarrow \mathbb{R}$ to evaluate whether a exceed its bound \bar{a}

$$\mathcal{M}(a, \bar{a}) = a - \bar{a}. \quad (33)$$

Thus, for each $n \in [1, \dots, N]$, we constrain the maximum velocity for the n^{th} aerial robot

$$\|\mathbf{v}_n\|^2 < v_{max}^2, \quad (34)$$

where v_{max} is the maximum allowable velocity of aerial robot. Then the penalty function for the constraint w.r.t in Eq. 34 is defined as

$$\mathcal{J}_v^n = \mathcal{L}_\mu \left(\mathcal{M}_{df}^{v_n} \left(\|\mathbf{v}_n\|^2, v_{max}^2 \right) \right). \quad (35)$$

In Eq. 35, a superscript v_n and a subscript df is added to the symbol \mathcal{M} to denote the dynamical constraint w.r.t this superscript. In the following of this paper, $\mathcal{M}_{df}^{v_n} \left(\|\mathbf{v}_n\|^2, v_{max}^2 \right)$ will be denoted by $\mathcal{M}_{df}^{v_n}$ for the sake of simplification. Finally, the gradients of $\mathcal{M}_{df}^{v_n}$ w.r.t \mathbf{c}_m, T_m can be computed as

$$\frac{\partial \mathcal{M}_{df}^{v_n}}{\partial \mathbf{c}_{m, \mathbf{p}}} = \left(\frac{\partial \mathcal{M}_{df}^{v_n}}{\partial \dot{\mathbf{p}}} \right)^T \otimes \beta, \quad (36a)$$

$$\frac{\partial \mathcal{M}_{df}^{v_n}}{\partial \mathbf{c}_{m, \rho_n}} = \sum_{j \in \Pi_v} \left[\left(\frac{\partial \mathcal{M}_{df}^{v_n}}{\partial \dot{\rho}_n} \right)^T \frac{\partial \dot{\rho}_n}{\partial \Phi_n^{(j)}} \right] \otimes \beta^{(j)}, \quad (36b)$$

$$\frac{\partial \mathcal{M}_{df}^{v_n}}{\partial \mathbf{c}_{m, F_n}} = \mathbf{0}, \quad (36c)$$

$$\begin{aligned} \frac{\partial \mathcal{M}_{df}^{v_n}}{\partial T_m} &= \left(\frac{\partial \mathcal{M}_{df}^{v_n}}{\partial \dot{\rho}_n} \right)^T \sum_{j \in \Pi_v} \frac{\partial \dot{\rho}_n}{\partial \Phi_n^{(j)}} \Phi_n^{(j+1)} \\ &+ \left(\frac{\partial \mathcal{M}_{df}^{v_n}}{\partial \dot{\mathbf{p}}} \right)^T \ddot{\mathbf{p}}, \end{aligned} \quad (36d)$$

where $\Pi_v = \{0, 1\}$ is an index set related to this constraint.

2) *Maximum and Minimum Thrust Constraint:* A realistic aerial robot can only provide a limited thrust. Therefore, to ensure the system controllability, for all $n \in [1, \dots, N]$, we restrict the mass-normalized thrust $\|\mathbf{f}_n\|$ to be less than the maximum thrust f_{max} that can be provided by a practical aerial robot and more than the minimum thrust f_{min}

$$f_{min} \leq \|\mathbf{f}_n\| \leq f_{max}. \quad (37)$$

Let f_{avg} denote $(f_{max} + f_{min})/2$, and f_{rag} denote $(f_{max} - f_{min})/2$, the penalty function for the constraint in Eq. 37 is defined as

$$\mathcal{J}_f^n = \mathcal{L}_\mu \left(\mathcal{M}_{df}^{f_n} \left((\|\mathbf{f}_n\| - f_{avg})^2, f_{rag} \right) \right). \quad (38)$$

Then the gradients of $\mathcal{M}_{df}^{f_n}$ w.r.t \mathbf{c}_m, T_m can be calculated as

$$\frac{\partial \mathcal{M}_{df}^{f_n}}{\partial \mathbf{c}_{m, \mathbf{p}}} = \left[\left(\frac{\partial \mathcal{M}_{df}^{f_n}}{\partial \mathbf{f}_n} \right)^T \frac{\partial \mathbf{f}_n}{\partial \dot{\mathbf{p}}} \right] \otimes \beta, \quad (39a)$$

$$\frac{\partial \mathcal{M}_{df}^{f_n}}{\partial \mathbf{c}_{m, \rho_n}} = \sum_{i \in \Pi_f} \sum_{j=0}^i \left[\left(\frac{\partial \mathcal{M}_{df}^{f_n}}{\partial \mathbf{f}_n} \right)^T \frac{\partial \mathbf{f}_n}{\partial \rho_n^{(i)}} \frac{\partial \rho_n^{(i)}}{\partial \Phi_n^{(j)}} \right] \otimes \beta^{(j)}, \quad (39b)$$

$$\frac{\partial \mathcal{M}_{df}^{f_n}}{\partial \mathbf{c}_{m, F_n}} = \left[\left(\frac{\partial \mathcal{M}_{df}^{f_n}}{\partial \mathbf{f}_n} \right)^T \frac{\partial \mathbf{f}_n}{\partial F_n} \right] \beta, \quad (39c)$$

$$\begin{aligned} \frac{\partial \mathcal{M}_{df}^{f_n}}{\partial T_m} &= \sum_{i \in \Pi_f} \sum_{j=0}^i \left(\frac{\partial \mathcal{M}_{df}^{f_n}}{\partial \mathbf{f}_n} \right)^T \frac{\partial \mathbf{f}_n}{\partial \rho_n^{(i)}} \frac{\partial \rho_n^{(i)}}{\partial \Phi_n^{(j)}} \Phi_n^{(j+1)} \\ &+ \left(\frac{\partial \mathcal{M}_{df}^{f_n}}{\partial \mathbf{f}_n} \right)^T \left(\frac{\partial \mathbf{f}_n}{\partial \dot{\mathbf{p}}} \ddot{\mathbf{p}} + \frac{\partial \mathbf{f}_n}{\partial F_n} \dot{F}_n \right). \end{aligned} \quad (39d)$$

where the index set $\Pi_f = \{0, 2\}$.

3) *Maximum Tilt Angle Constraints:* For each $n \in [1, \dots, N]$, we limit the maximum tilt angle ϑ_n for the n^{th} aerial robot

$$\vartheta_n \leq \vartheta_{max}, \quad (40)$$

where ϑ_{max} is the maximum admissible tilt angle. Thus, the penalty function for the constraint in Eq. 40 can be defined as

$$\mathcal{J}_\vartheta^n = \mathcal{L}_\mu \left(\mathcal{M}_{df}^{\vartheta_n} (\vartheta_n, \vartheta_{max}) \right). \quad (41)$$

Since $\mathcal{M}_{df}^{\vartheta_n}$ relies on \mathbf{f}_n as $\mathcal{M}_{df}^{f_n}$, the formulation of $\frac{\partial \mathcal{M}_{df}^{\vartheta_n}}{\partial \mathbf{c}_m} \frac{\partial \mathcal{M}_{df}^{\vartheta_n}}{\partial T_m}$ is similar to Eq. 39a - Eq. 39d except that $\mathcal{M}_{df}^{f_n}$ need to be substituted by $\mathcal{M}_{df}^{\vartheta_n}$ and $\frac{\partial \mathcal{M}_{df}^{\vartheta_n}}{\partial \mathbf{f}_n}$ can be computed by

$$\frac{\partial \mathcal{M}_{df}^{\vartheta_n}}{\partial \mathbf{f}_n} = \sum_{i \in \Pi_\vartheta} \frac{\partial \mathcal{M}_{df}^{\vartheta_n}}{\partial q_n^i} \left(\frac{\partial q_n^i}{\partial \mathbf{z}_B} \right)^T \frac{\mathbf{z}_B^n}{\partial \mathbf{f}_n}, \quad (42)$$

where the index set $\Pi_\vartheta = \{x, y\}$.

4) *Maximum Body Rate Constraint*: For each $n \in [1, \dots, N]$, we restrict the upper bound of body rate

$$\|\boldsymbol{\omega}_n\| \leq \omega_{max}, \quad (43)$$

where ω_{max} is the maximum admissible body rate for aggressive flight. The penalty function for the constraint in Eq. 43 is defined as

$$\mathcal{J}_\omega^n = \mathcal{L}_\mu \left(\mathcal{M}_{df}^{\omega_n} (\|\boldsymbol{\omega}_n\|^2, \omega_{max}^2) \right). \quad (44)$$

And the gradients of $\mathcal{M}_{df}^{\omega_n}$ w.r.t \mathbf{c}_m, T_m are computed as

$$\frac{\partial \mathcal{M}_{df}^{\omega_n}}{\partial \mathbf{c}_{m, \mathbf{P}}} = \sum_{i \in \Pi_\omega} \left[\left(\frac{\partial \mathcal{M}_{df}^{\omega_n}}{\partial \mathbf{f}_n^{(i)}} \right)^T \frac{\partial \mathbf{f}_n^{(i)}}{\partial \mathbf{p}^{(i+2)}} \right] \otimes \boldsymbol{\beta}^{(i+2)}, \quad (45a)$$

$$\frac{\partial \mathcal{M}_{df}^{\omega_n}}{\partial \mathbf{c}_{m, \rho_n}} = \sum_{i \in \Pi_\omega} \sum_{j \in \Pi_\omega^i} \sum_{k=0}^j \left[\left(\frac{\partial \mathcal{M}_{df}^{\omega_n}}{\partial \mathbf{f}_n^{(i)}} \right)^T \frac{\partial \mathbf{f}_n^{(i)}}{\partial \rho_n^{(j)}} \frac{\partial \rho_n^{(j)}}{\partial \Phi_n^{(k)}} \right] \otimes \boldsymbol{\beta}^{(k)}, \quad (45b)$$

$$\frac{\partial \mathcal{M}_{df}^{\omega_n}}{\partial \mathbf{c}_{m, F_n}} = \sum_{i \in \Pi_\omega} \sum_{j=0}^i \left[\left(\frac{\partial \mathcal{M}_{df}^{\omega_n}}{\partial \mathbf{f}_n^{(i)}} \right)^T \frac{\partial \mathbf{f}_n^{(i)}}{\partial F_n^{(j)}} \right] \boldsymbol{\beta}^{(j)}, \quad (45c)$$

$$\begin{aligned} \frac{\partial \mathcal{M}_{df}^{\omega_n}}{\partial T_m} &= \sum_{i \in \Pi_\omega} \sum_{j \in \Pi_\omega^i} \sum_{k=0}^j \left(\frac{\partial \mathcal{M}_{df}^{\omega_n}}{\partial \mathbf{f}_n^{(i)}} \right)^T \frac{\partial \mathbf{f}_n^{(i)}}{\partial \rho_n^{(j)}} \frac{\partial \rho_n^{(j)}}{\partial \Phi_n^{(k)}} \Phi_n^{(k+1)} \\ &+ \sum_{i \in \Pi_\omega} \sum_{j=0}^i \left(\frac{\partial \mathcal{M}_{df}^{\omega_n}}{\partial \mathbf{f}_n^{(i)}} \right)^T \frac{\partial \mathbf{f}_n^{(i)}}{\partial F_n^{(j)}} F_n^{(j+1)} \\ &+ \sum_{i \in \Pi_\omega} \left(\frac{\partial \mathcal{M}_{df}^{\omega_n}}{\partial \mathbf{f}_n^{(i)}} \right)^T \frac{\partial \mathbf{f}_n^{(i)}}{\partial \mathbf{p}^{(i+2)}} \mathbf{p}^{(i+3)}, \end{aligned} \quad (45d)$$

where the index sets are defined respectively as $\Pi_\omega = \{0, 1\}$, $\Pi_\omega^0 = \{0, 2\}$, $\Pi_\omega^1 = \{0, 1, 3\}$. Besides, for any $i \in \Pi_\omega$, $\frac{\partial \mathcal{M}_{df}^{\omega_n}}{\partial \mathbf{f}_n^{(i)}}$ can be further calculated as

$$\frac{\partial \mathcal{M}_{df}^{\omega_n}}{\partial \mathbf{f}_n^{(i)}} = \sum_{j=i}^1 \left(\frac{\partial \mathcal{M}_{df}^{\omega_n}}{\partial \boldsymbol{\omega}_n} \right)^T \frac{\partial \boldsymbol{\omega}_n}{\partial \mathbf{z}_B^{(j)}} \frac{\mathbf{z}_B^{(j)}}{\partial \mathbf{f}_n^{(i)}}. \quad (46)$$

E. Coupling Dynamic Constraint

As has exposted in Sec. III-D, we need to enforce an extra payload dynamical constraint on the extended flat-output variable \mathbf{Z} based on Eq. 1b

$$\dot{\mathbf{v}} \equiv -g\mathbf{e}_3 + \sum_{n=1}^N F_n \boldsymbol{\rho}_n / m_L. \quad (47)$$

Then we construct the penalty function for this constraint

$$\mathcal{J}_d = \mathcal{M} \left(\left\| \ddot{\mathbf{p}} + g\mathbf{e}_3 - \sum_{n=1}^N F_n \boldsymbol{\rho}_n / m_L \right\|, 0 \right). \quad (48)$$

Denoted by \mathcal{M}_{cd} the right hand of Eq. 47, and the gradients of \mathcal{M}_{cd} w.r.t \mathbf{c}_m, T_m are computed as

$$\frac{\partial \mathcal{M}_{cd}}{\partial \mathbf{c}_p} = \left(\frac{\partial \mathcal{M}_{cd}}{\partial \ddot{\mathbf{p}}} \right)^T \otimes \ddot{\boldsymbol{\beta}}, \quad (49a)$$

$$\frac{\partial \mathcal{M}_{cd}}{\partial \mathbf{c}_{m, \rho_n}} = \left[\left(\frac{\partial \mathcal{M}_{cd}}{\partial \rho_n} \right)^T \frac{\partial \rho_n}{\partial \Phi_n} \right] \otimes \boldsymbol{\beta}, \quad (49b)$$

$$\frac{\partial \mathcal{M}_{cd}}{\partial \mathbf{c}_{m, F_n}} = \frac{\partial \mathcal{M}_{cd}}{\partial F_n} \boldsymbol{\beta}, \quad (49c)$$

$$\begin{aligned} \frac{\partial \mathcal{M}_{cd}}{\partial T_m} &= \sum_{n=1}^N \left[\left(\frac{\partial \mathcal{M}_{cd}}{\partial \rho_n} \right)^T \frac{\partial \rho_n}{\partial \Phi_n} \dot{\Phi}_n + \frac{\partial \mathcal{M}_{cd}}{\partial F_n} \dot{F}_n \right] \\ &+ \left(\frac{\partial \mathcal{M}_{cd}}{\partial \ddot{\mathbf{p}}} \right)^T \ddot{\mathbf{p}}. \end{aligned} \quad (49d)$$

F. Cable's Vectorial Constraints

Considering an acceleration \mathbf{a} and a set $F = \{F_1 \boldsymbol{\rho}_1, \dots, F_N \boldsymbol{\rho}_N\}$ that contains all cables's force vectors satisfying Eq. 1b, we find that \mathbf{a} and a new set $F' = \{R(\phi) F_1 \boldsymbol{\rho}_1, \dots, R(\phi) F_N \boldsymbol{\rho}_N\}$ obtained by rotating all the vectors in F around the vector $\mathbf{a} + g\mathbf{e}_3$ by an arbitrary angle ϕ , still satisfy Eq. 1b, where $R(\phi) \in SO(3)$ is the rotation matrix. Besides, from Eq. 1b, we also conclude that the set $F'' = \{F_{\sigma(1)} \boldsymbol{\rho}_{\sigma(1)}, \dots, F_{\sigma(N)} \boldsymbol{\rho}_{\sigma(N)}\}$ obtained by commuting the force vectors among the cables, doesn't vary the payload's dynamics, where $\sigma: \mathcal{Z}^+ \rightarrow \mathcal{Z}^+$ is the index commutation operator. Infinite feasible sets like F' and F'' increase the possibility of the optimization variables getting trapped in local optimums, which gives rise to undesirable trajectories.

To alleviate the local optima and speed up the convergence of the optimization, we separate the vectorial range of the cables and limit the optimization of each force vector within its own vectorial range. Concretely, for each $n \in [1, \dots, N]$, we construct the following vectorial constraints

$$0 \leq \theta_n \leq \theta_{max}, \quad (50a)$$

$$-\frac{(2n-3)\pi}{N} \leq \phi_n \leq \frac{(2n-1)\pi}{N}, \quad (50b)$$

where θ_{max} is the maximum allowable pitch angle of the cable. Besides, we also enforce the constraint on each cable's force F_n

$$F_{min} \leq F_n \leq F_{max}, \quad (51)$$

where F_{min}, F_{max} are respectively the minimum and maximum allowable forces of the cable. This constraint prevents the cable from being slack and providing an excessive force compared to other cables.

V. SPATIAL-TEMPORAL TRAJECTORY OPTIMIZATION

A. System-level Path Planning

To provide a reasonable initial path for trajectory optimization, we design a system-level global path planning method. The MARTS is simplified to a mobile and scalable regular pyramid and the length of its lateral edge is equal to the length of the cable. As shown in Fig. 4, γ is defined as the scalable variable used to regulate the size of the regular polygon base. Let \mathcal{C}_{rp} be the configuration space of this regular pyramid, thus given the payload's position \mathbf{p} and γ , any configuration in \mathcal{C}_{rp} can be uniquely represented by an ordered pair (\mathbf{p}, γ) . We discretize \mathcal{C}_{rp} and use A^* algorithm to obtain a collision-free path. A collision-free configuration on this path signifies that

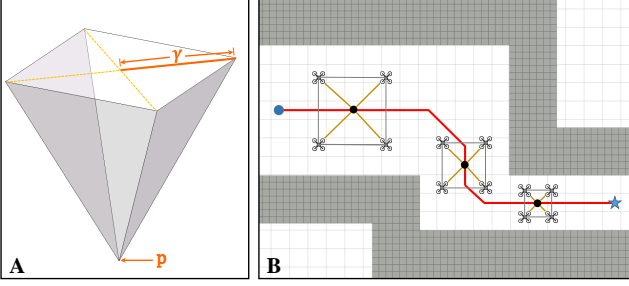


Fig. 4. Illustration of the system-level path planning method proposed in Sec. V-A. (A) The simplified configuration of the MARTS. (B) The simplified configuration is scaled to fit different widths of the corridor.

the entire regular pyramid with γ at point \mathbf{p} doesn't collide with any environmental obstacle. We use a solid, convex, and even conservative regular pyramid instead of a hollow, non-convex compact geometry just enveloping the entire MARTS to check the collision such that a safe corridor is not penetrated by any obstacle can be opened up by uniting the consecutive convex regular pyramids for trajectory deformation in the back-end optimization.

B. Trajectory Optimization Problem Formulation

The trajectory optimization problem of SAAT can be formulated as follows

$$\min_{\mathbf{w}, \mathbf{T}} \mathcal{J}_E = \int_0^T \|\mathbf{p}^{(s)}(t)\|^2 dt + \lambda_Z \sum_{n=1}^N \int_0^T \|\xi_n^{(s)}(t)\|^2 dt + \lambda_T T_\Sigma, \quad (52a)$$

$$s.t. \quad (\mathbf{c}, \mathbf{T}) = \mathcal{L}(\mathbf{w}, \mathbf{T}), \quad (52b)$$

$$T_m > 0, \quad \forall m \in [1, \dots, M], \quad (52c)$$

$$\mathbf{Z}^{[s-1]}(0) = \bar{\mathbf{Z}}_0, \quad (52d)$$

$$\mathbf{Z}^{[s-1]}(T_\Sigma) = \bar{\mathbf{Z}}_{T_\Sigma}, \quad (52e)$$

$$\mathcal{G}(\mathbf{Z}^{[s-1]}(t)) \preceq \mathbf{0}, \quad \forall t \in [0, T_\Sigma], \quad (52f)$$

$$\mathcal{H}(\mathbf{Z}^{[s-1]}(t)) = \mathbf{0}, \quad \forall t \in [0, T_\Sigma], \quad (52g)$$

where $T_\Sigma = \sum_{m=1}^M T_m$. Cost function (52a) compromises the smoothness and agility of the trajectory $\mathbf{Z}(t)$, λ_Z regulates the smoothness of the aerial robot's motion related to the load, and λ_T is the time regularization parameter. Eq. 52b restricts that the parameters $\{\mathbf{c}, \mathbf{T}\}$ representing $\mathbf{Z}(t)$ can only be mapped by sparse optimization variables \mathbf{w}, \mathbf{T} provided by $\mathcal{C}_{\text{MINCO}}$. Eq. 52c guarantees the duration of each piece is positive. Eq. 52d and Eq. 52e set the trajectory's boundary conditions. Eq. 52f denotes the inequality constraints continuously imposed along the trajectory, and Eq. 52g are additional equality constraints designed to ensure that the flat-output trajectory $\mathbf{Z}(t)$ complies with the payload's dynamics.

Then, we derive the formulations of \mathcal{J}_E gradient w.r.t \mathbf{c}_m, T_m as

$$\frac{\partial \mathcal{J}_E}{\partial \mathbf{c}_m, \mathbf{p}} = 2 \left(\int_0^{T_m} \beta^{(s)}(t) \beta^{(s)}(t)^T dt \right) \mathbf{c}_m, \mathbf{p}, \quad (53a)$$

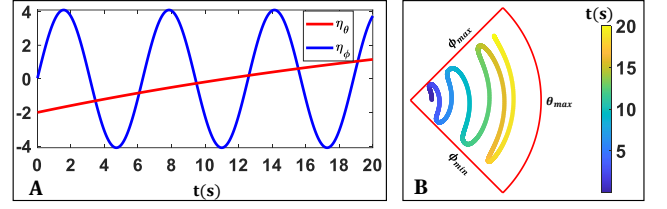


Fig. 5. Illustration of the diffeomorphism defined in Eq. 54. (A) The selected trajectories for the auxiliary variables $\eta_\theta \in \mathbb{R}, \eta_\phi \in \mathbb{R}$ to solve the trajectories of θ, ϕ by Eq. 54. (B) The trajectory of ρ_n solved by Eq. 5 using the trajectories of θ, ϕ can always be compressed into a bounded red fan-shaped region.

$$\frac{\partial \mathcal{J}_E}{\partial \mathbf{c}_m, \xi_n} = 2\lambda_Z \left(\int_0^{T_m} \beta^{(s)}(t) \beta^{(s)}(t)^T dt \right) \mathbf{c}_m, \xi_n, \quad (53b)$$

$$\frac{\partial \mathcal{J}_E}{\partial T_m} = \left\| \mathbf{p}^{(s)}(T_m) \right\|^2 + \lambda_Z \sum_{n=1}^N \left\| \xi_n^{(s)}(T_m) \right\|^2 + \lambda_T. \quad (53c)$$

C. Constraints Elimination

The infinite number of constraints are introduced since the inequality (Eq. 52f) and the equality (Eq. 52g) are enforced over the trajectory's entire duration T_Σ , leading to difficulties in solving the optimization problem (Eq. 52). Therefore, to simplify this optimization problem, we design approaches to eliminate these infinite number of constraints as well as the temporal constraints (Eq. 52c) as follows.

1) *Vectorial Constraint Elimination*: The vectorial constraints (Eq. 50 - Eq. 51) enforced on the n^{th} force vector are constructed directly on ξ_n , so that for each $m' \in [1, \dots, M-1]$, we can eliminate these constraints enforced at the m'^{th} junction $\xi_n^{m'}$ in $\mathbf{w}_{m'}$ between the m'^{th} piece and the $(m'+1)^{\text{th}}$ piece of trajectory via designing a smooth diffeomorphism $\mathcal{S} : \mathbb{R} \rightarrow \mathbb{R}$. That is, let us introduce an auxiliary variable $\eta_n^{m'} \in \mathbb{R}^3$, and for each element $\xi \in \xi_n^{m'}$, we select the same element $\eta \in \eta_n^{m'}$ to map ξ as

$$\xi = \mathcal{S}(\eta) = \frac{\xi_{\min} + \xi_{\max}}{2} + \frac{(\xi_{\max} - \xi_{\min})}{\pi} \arctan \eta, \quad (54)$$

where ξ_{\min}, ξ_{\max} are respectively the lower and upper bounds of ξ . \mathcal{S} maps \mathbb{R} to interval $[\xi_{\min}, \xi_{\max}]$ such that arbitrary optimization of η on \mathbb{R} always guarantees $\xi \in [\xi_{\min}, \xi_{\max}]$.

Then the gradient of any penalty function \mathcal{J} w.r.t η can be computed as

$$\frac{\partial \mathcal{J}}{\partial \eta} = \frac{\xi_{\max} - \xi_{\min}}{\pi(\eta^2 + 1)} \frac{\partial \mathcal{J}}{\partial \xi}. \quad (55)$$

2) *Temporal Constraint Elimination*: In order to eliminate the constraint Eq. 52c on T_m , we introduce $\tau = [\tau_1, \dots, \tau_M]^T \in \mathbb{R}^M$ as an auxiliary temporal vector and define the following diffeomorphism to map T_m from τ_m

$$T_m = e^{\tau_m}, \quad (56)$$

such that optimizing τ_m over \mathbb{R} always guarantees $T_m > 0$.

3) *Infinite Continuous-time Constraint Elimination*: Inspired by work [42], to transform infinite inequality constraints to finite constraints, we adopt the constraint transcription by introducing a new integral-type constraint as

$$\mathcal{J}_G^f = \int_0^{T_\Sigma} \mathcal{J}_G dt \leq 0. \quad (57)$$

Since the analytic value of \mathcal{J}_G^f is always difficult to evaluate, we turn to approximating it by quadrature using uniformly sampled penalty functions along the trajectory as

$$\mathcal{J}_G^f \approx \mathcal{J}_G^\Sigma = \sum_{m=1}^M \mathcal{J}_{G,m}^\Sigma, \quad (58)$$

where $\mathcal{J}_{G,m}^\Sigma$ is the approximate quadrature for the m^{th} piece can be calculated as

$$\mathcal{J}_{G,m}^\Sigma = \frac{T_m}{\kappa} \sum_{k=0}^{\kappa} \bar{\omega}_k \mathcal{J}_G \left(\mathbf{z}_m^{[s-1]}(t_k) \right). \quad (59)$$

κ is the sampled number on each piece, $(\bar{\omega}_0, \bar{\omega}_1, \dots, \bar{\omega}_{\kappa_i-1}, \bar{\omega}_{\kappa_i}) = (1/2, 1, \dots, 1, 1/2)$ are the coefficients of the sampled penalty functions for the quadrature following the trapezoidal rule [43] and $t_k = \frac{k}{\kappa} T_m$. Then the gradients of $\mathcal{J}_{G,m}^\Sigma$ w.r.t. \mathbf{c}_m and T_m can be easily derived as

$$\frac{\partial \mathcal{J}_{G,m}^\Sigma}{\partial \mathbf{c}_m} = \frac{T_m}{\kappa} \sum_{k=0}^{\kappa} \bar{\omega}_k \frac{\partial \mathcal{J}_G \left(\mathbf{z}_m^{[s-1]}(t_k) \right)}{\partial \mathbf{c}_m}, \quad (60a)$$

$$\frac{\partial \mathcal{J}_{G,m}^\Sigma}{\partial T_m} = \frac{\mathcal{J}_{G,m}^\Sigma}{T_m} + \frac{T_m}{\kappa^2} \sum_{k=0}^{\kappa} k \bar{\omega}_k \frac{\partial \mathcal{J}_G \left(\mathbf{z}_m^{[s-1]}(t_k) \right)}{\partial t_k}. \quad (60b)$$

Since the DOF of optimization variable \mathbf{Z} related to coupling dynamic constraint (Eq. 47) is $3+3 \times N$, which is much larger than 3, i.e., the number of this constraint, we can make the trajectory approximately satisfy Eq. 47 by constructing a finite constraint $\mathcal{J}_H^f \leq 0$ similar to Eq. 58 - Eq. 59 and approximately calculate $\mathcal{J}_H^\Sigma, \mathcal{J}_{H,m}^\Sigma$ similar to Eq. 58 - Eq. 59. Besides, the gradients of $\mathcal{J}_{H,m}^\Sigma$ w.r.t. \mathbf{c}_m and T_m are similar to Eq. 60a - Eq. 60b, which are abandoned here.

D. Unconstrained NLP formation

After the elimination of the vectorial constraints in Sec. V-C1, the continuous-time penalty functions for SAAT in complex environments can be summarized as

$$\mathcal{J}_G = \sum_{n=0}^N \lambda_{oa} \mathcal{J}_{oa}^n + \sum_{v \in \Upsilon} \sum_{n=1}^N \lambda_v \mathcal{J}_v^n + \lambda_{ra} \mathcal{J}_{ra}, \quad (61a)$$

$$\mathcal{J}_H = \lambda_d \mathcal{J}_d, \quad (61b)$$

where the set of subscript is defined as $\Upsilon = \{\mathbf{v}, \mathbf{f}, \vartheta, \boldsymbol{\omega}\}$. $\lambda_{oa}, \lambda_{ra}, \lambda_v, \lambda_f, \lambda_\vartheta$, and λ_ω are preset weights for the penalty functions. Besides, the actual sparse trajectory parameters $\{\mathbf{w}, \mathbf{T}\}$ will be substituted by the auxiliary sparse parameters $\{\boldsymbol{\varpi}, \boldsymbol{\tau}\}$, where $\boldsymbol{\varpi} = (\boldsymbol{\varpi}_1, \dots, \boldsymbol{\varpi}_{M-1})^T \in \mathbb{R}^{(4N+3) \times (M-1)}$ and for any $m' \in [1, \dots, M-1]$, $\boldsymbol{\varpi}_{m'} \in \mathbb{R}^{4N+3}$ can be denoted by $\boldsymbol{\varpi}_{m'} = (\mathbf{p}^{m'T}, \boldsymbol{\eta}_1^{m'T}, \psi_1^{m'}, \dots, \boldsymbol{\eta}_N^{m'T}, \psi_N^{m'})^T$.

Then, based on the constraint elimination introduced in Sec. V-C3, we convert original optimization problem defined in Eq. 52 to an unconstrained optimization problem

$$\min_{\boldsymbol{\varpi}, \boldsymbol{\tau}} \mathcal{J}_E + \sum_{m=1}^M (\mathcal{J}_{G,m}^\Sigma + \mathcal{J}_{H,m}^\Sigma). \quad (62)$$

This problem can be efficiently solved by fast spatio-temporal deformation provided by $\mathcal{C}_{\text{MINCO}}$. Each deformation involves the following two procedures as shown in Fig. 2. In the forward trajectory generation, $\{\mathbf{w}, \mathbf{T}\}$ is firstly mapped from $\{\boldsymbol{\varpi}, \boldsymbol{\tau}\}$, then $\mathcal{C}_{\text{MINCO}}$ use the banded matrix PLU decomposition to solve Eq. 18, acquiring $\{\mathbf{c}, \mathbf{T}\}$ from $\{\mathbf{w}, \mathbf{T}\}$. Besides, in the backward gradient propagation, through ingenious reuse of the solved PLU matrixes, $\mathcal{C}_{\text{MINCO}}$ avoids the inversion of a $2sM$ -dimensional matrix such that the gradients $\{\frac{\partial \mathcal{J}}{\partial \mathbf{c}}, \frac{\partial \mathcal{J}}{\partial \mathbf{T}}\}$ are firstly propagated to $\{\frac{\partial \mathcal{J}}{\partial \mathbf{w}}, \frac{\partial \mathcal{J}}{\partial \mathbf{T}}\}$ and further propagated to $\{\frac{\partial \mathcal{J}}{\partial \boldsymbol{\varpi}}, \frac{\partial \mathcal{J}}{\partial \boldsymbol{\tau}}\}$. Both the two processes rely just on linear spatio-temporal computational complexity. Thus, fast spatio-temporal deformation of trajectory will be performed via the updation of $\{\boldsymbol{\varpi}, \boldsymbol{\tau}\}$.

VI. CONTROL SCHEME FOR AGILE TRANSPORTATION

In this work, we propose a robust and distributed control scheme to achieve agile transportation, the architecture of which is shown at the bottom of Fig. 2. It should be pointed out that in this section, we add n to the superscript or subscript of symbols to specify that they belong to the n^{th} aerial robot, but for simplicity, we omit n in Fig. 2. This scheme gets rid of the reliance on the state measurement for both payload and cable as in works [29]–[32], as well as the closed-loop control for payload as in works [27]–[32]. Instead, it pursues closed-loop control for each aerial robot. That's to say the position and velocity errors of the payload would not be considered in the aerial robot's control law such that the system oscillation induced by the payload's control law and time-delay induced by control signal transmission can be avoided fundamentally. INDI is used to estimate the direction and magnitude of the tension in each cable such that we don't need to deploy additional tension sensors or attitude sensors to measure these states, and the unknown payload's mass can be online estimated. Both the actual estimation for the cable's force vector and planned trajectory are used to calculate the flatness maps and further get the desired states. Since the INDI always compensates the actual force exerted by the cable, this control scheme is robust against the deviations from the planned trajectory, which are introduced by the payload's swing around the cables' attachment point induced by the inevitable attachment error and the estimation error of the payload's mass. The details about the outer-loop trajectory tracking controller and the inner-loop geometric attitude controller contained in this scheme are as follows.

A. Outer Loop Controller

Before we derive the control law, the actual mass-normalized thrust f_n and control torque $\boldsymbol{\tau}_n$ of the n^{th} aerial robot should be firstly estimated by the mixing matrix using the RPMs of motors, i.e., $r_{n,1}, \dots, r_{n,4}$.

For the outer loop, the external forces that each aerial robot suffers from, such as the actual tension exerted by the cable and the aerodynamic drags are considered as a whole. The feedforward trajectory tracking control law for the n^{th} aerial robot is calculated as

$$\mathbf{a}_{n,c} = K_p(\mathbf{p}_{n,d} - \mathbf{p}_n) + K_v(\mathbf{v}_{n,d} - \mathbf{v}_n) + \mathbf{a}_{n,d}. \quad (63)$$

Based on the principle of INDI, the mass-normalized thrust vector command $\mathbf{f}_{n,c}$ that provides $\mathbf{a}_{n,c}$ can be computed using the following incremental relation

$$\mathbf{f}_{n,c} = \mathcal{FL}(f_n \mathbf{z}_{\mathcal{B}}^n) + \mathbf{a}_{n,c} - \mathcal{FL}(\mathbf{a}_n), \quad (64)$$

where $\mathcal{FL}()$ is a low-pass filter. Then the mass-normalized thrust command $f_{n,c}$ and its unit vector direction $\mathbf{z}_{\mathcal{B},c}^n$ are obtained as

$$f_{n,c} = \|\mathbf{f}_{n,c}\|_2, \quad \mathbf{z}_{\mathcal{B},c}^n = \mathcal{N}(\mathbf{f}_{n,c}). \quad (65)$$

Besides, the tension $-\widetilde{F}_n \widetilde{\boldsymbol{\rho}}_n$ exerted on the n^{th} aerial robot by the n^{th} cable is estimated by rewriting Eq. 2b as follows

$$-\widetilde{F}_n \widetilde{\boldsymbol{\rho}}_n = -m_n(\mathcal{FL}(\mathbf{a}_n) - g\mathbf{e}_3 + \mathcal{FL}(f_n \mathbf{z}_{\mathcal{B}}^n)). \quad (66)$$

Then, the n^{th} cable's tension F_n and the vector direction $\boldsymbol{\rho}_n$ can be estimated as

$$\widetilde{F}_n = \|\widetilde{F}_n \widetilde{\boldsymbol{\rho}}_n\|_2, \quad \widetilde{\boldsymbol{\rho}}_n = \mathcal{N}(\widetilde{F}_n \widetilde{\boldsymbol{\rho}}_n). \quad (67)$$

It should be pointed out that $-\widetilde{F}_n \widetilde{\boldsymbol{\rho}}_n$ contains not only the n^{th} cable's tension but also the disturbances such as the wind and the aerodynamic drag that the aerial robot suffers from.

B. Inner Loop Controller

For the inner loop, since it is generally not possible to tie a cable strictly to the CoM of the aerial robot, the INDI is also used to compensate for the inevitable external moment induced by the cable. Based on the desired yaw angle $\psi_{n,d}$ and the unit vector direction of the thrust, we reconstruct the desired attitude $\mathbf{q}_{n,d}$ using the rotation factorization provided by Hopf fibration

$$\mathbf{q}_{n,d} = \mathbf{q}_{\mathbf{z}_{\mathcal{B},c}^n} \odot \mathbf{q}_{\psi_{n,d}}. \quad (68)$$

Then the quaternion $\mathbf{q}_{n,e}$ representing the rotation to align the desired attitude $\mathbf{q}_{n,d}$ to current attitude \mathbf{q}_n is calculated as

$$\mathbf{q}_{n,e} = \mathbf{q}_n^{-1} \odot \mathbf{q}_{n,d}. \quad (69)$$

$\mathbf{q}_{n,e}$ implies a rotation around an axis $\boldsymbol{\ell}_n$ denoted by $\ell_n = (\mathbf{q}_{n,e}^x, \mathbf{q}_{n,e}^y, \mathbf{q}_{n,e}^z)^T$, thus we define a vector $\boldsymbol{\Theta}_{n,e}$ to describe this rotation as

$$\boldsymbol{\Theta}_{n,e} = 2 \arccos(\mathbf{q}_{n,e}^w) \mathcal{N}(\boldsymbol{\ell}_n). \quad (70)$$

Next, the attitude tracking control law $\dot{\boldsymbol{\omega}}_{n,c}$ is designed as

$$\dot{\boldsymbol{\omega}}_{n,c} = K_{\boldsymbol{\Theta}} \boldsymbol{\Theta}_{n,e} + K_{\boldsymbol{\omega}}(\boldsymbol{\omega}_{n,e}) + K_I \int \boldsymbol{\omega}_{n,e} dt + \dot{\boldsymbol{\omega}}_{n,d}. \quad (71)$$

where $\boldsymbol{\omega}_{n,e}$ is the error of body rate that can be calculated as

$$\boldsymbol{\omega}_{n,e} = \mathbf{q}_n^{-1} \odot \mathbf{q}_{n,d} \odot \boldsymbol{\omega}_{n,d} - \mathcal{FL}(\boldsymbol{\omega}_n). \quad (72)$$

Note that the desired body rate $\boldsymbol{\omega}_{n,d}$ is calculated by Eq. 15a - Eq. 15c based on the states getting from the trajectory except

TABLE II
PARAMETER SETTING FOR SIMULATIONS AND EXPERIMENTS

System Parameter					
m_i	320g	l	1.2m		
J_i	$\text{diag}(4.463, 4.725, 5.340) \times 10^{-4} \text{kg} \cdot \text{m}^2$				
Planning Parameter					
d_{oa}^L	0.2m	d_{oa}^Q	0.3m	d_{oa}^c	0.2m
K	7	d_s	0.2m	v_{max}	6.0m/s
f_{max}	30N/kg	ϑ_{max}	1.05rad	ω_{max}	2.7rad/s
θ_{max}	1.0rad	F_{min}	0.24N	F_{max}	2.4N
λ_T	2000.0	λ_z	0.3	λ_{oa}	10000.0
λ_{ra}	10000.0	λ_v	1000.0	λ_τ	1000.0
λ_ω	1000.0	λ_ϑ	1000.0	λ_ζ	10000.0
Control Parameter					
cof	20Hz	W	1000		
K_p	$\text{diag}(12.0, 12.0, 3.0)$		K_v	$\text{diag}(4.0, 4.0, 2.0)$	
$K_{\boldsymbol{\Theta}}$	$\text{diag}(70.0, 100.0, 19.0)$		K_ω	$\text{diag}(10.0, 12.0, 3.0)$	
K_I	$\text{diag}(0.0, 0.0, 0.3)$				

that $F_n, \boldsymbol{\rho}_n$ used to calculate $\mathbf{z}_{\mathcal{B}}^n$ (Eq. 9) and $\mathbf{z}_{\mathcal{B}}^n$ (Eq. 16a) are substituted by their estimations $F_n, \widetilde{\boldsymbol{\rho}}_n$. From the primitive of INDI, the incremental expression for the moment command can be computed as

$$\boldsymbol{\tau}_{n,c} = \mathcal{FL}(\boldsymbol{\tau}_n) + \mathbf{J}_n(\dot{\boldsymbol{\omega}}_{n,c} - \dot{\boldsymbol{\omega}}_n). \quad (73)$$

It should be pointed out that the low-pass filters for $\mathbf{a}_n, f_n \mathbf{z}_{\mathcal{B}}^n, \boldsymbol{\omega}_n$ and $\boldsymbol{\tau}_n$ are set to the same cut-off frequency cof .

C. Estimation for Mass of Payload

When the payload is lifted, the MARTS will be stabilized at a predefined position. Then the mass of the payload can be estimated by a finite sequence of each aerial robot's estimations for the force vector of the cable attached to it as follows

$$\widetilde{m}_L = \sum_{n=1}^N \sum_{w=1}^W \frac{\widetilde{F}_n \widetilde{\boldsymbol{\rho}}_n|_{w,3}}{W}. \quad (74)$$

where $\widetilde{F}_n \widetilde{\boldsymbol{\rho}}_n|_{w,3}$ denotes the z component of the w^{th} estimation for $F_n \boldsymbol{\rho}_n$ in the sequence and W denotes the number of the estimations in the sequence.

VII. BENCHMARKS AND SIMULATIONS

In this section, benchmarks and simulations are carried out to validate our proposed trajectory planning scheme for SAAT

TABLE III
PERFORMANCE COMPARISON BETWEEN THE TWO METHODS

Scenario	Method	success rate(%)	length(m)
Sparse	Wahba's	83.3	22.069
	Ours	100	21.422
Medium	Wahba's	66.8	23.477
	Ours	100	21.568
Dense	Wahba's	44.5	25.282
	Ours	100	22.211

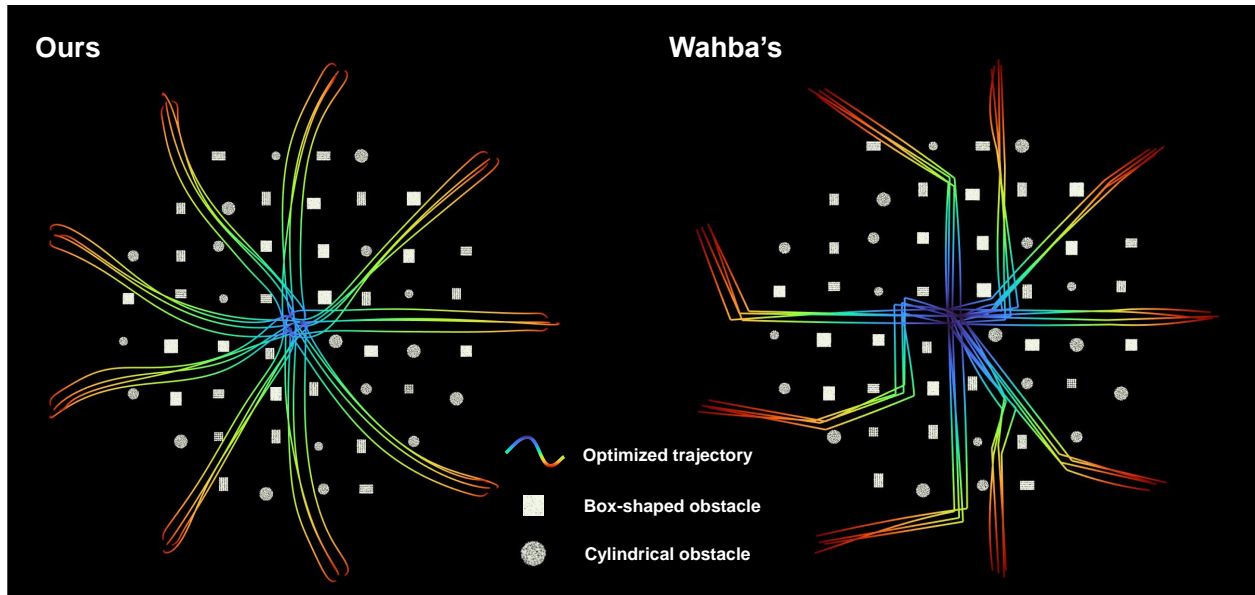


Fig. 6. Comparison of the partial trajectories in the medium-density environment optimized by the two methods.

in complex environments. First, we compare our planning scheme with a SOTA planner and analyze the performance in terms of responsiveness and trajectory quality (Sec. VII-A). Then, we conduct an ablation study (Sec. VII-B) to validate that the vectorial constraint (Eq. 50) enforced to the cable is indispensable to avoid undesirable locally optimal trajectory.

The optimization and visualization of the trajectories are implemented on a laptop with an Intel Core i5-10300H CPU (2.5 GHz) and don't depend on any hardware acceleration. The code implementation of our methods is based on C++11. Important parameters used for the following benchmarks, simulations in this section, and real-world experiments in Sec. VIII are shown in Tab. II.

A. Benchmark Comparisons

In this work, a SOTA kinodynamic motion planner for the payload transportation using MARTS proposed by Wahba et al. [26] is selected, which relies on the Flexible Collision Library [44] for collision checking and is implemented based on the differential dynamic programming [45] solver in Crocoddyl [46], to compare the performance with our trajectory planning scheme.

The first experiment tests the quality of the optimized trajectories planned by the two methods. Three circular environments with radii of 18m, featuring sparse, medium, and dense obstacle densities are constructed, among which the medium-density environment is shown in Fig. 6. We select the center of the circular environment as the starting point and uniformly choose 36 points on a circle with a radius of 21m as the target points to respectively plan 36 trajectories using the two methods. The bounds of the constraints considered in both methods are set to be the same as listed in Tab II. An optimized result is successful if the planner generates a dynamically feasible trajectory. For each obstacle density, we evaluate the two methods for the MARTS consisting of three

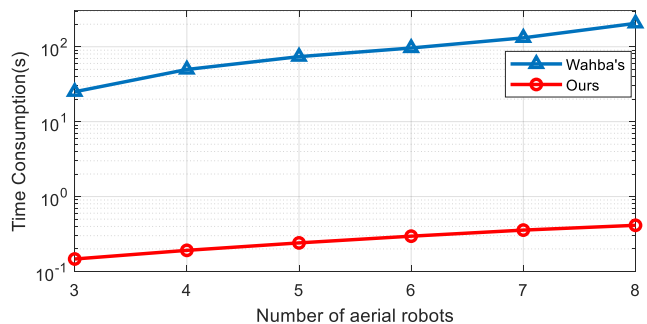


Fig. 7. Responsiveness comparison of the two methods.

aerial robots in terms of the success rate and the average length of these 36 trajectories.

The result is shown in Tab. III. As the density of obstacles increases, the success rate of Wahba's method significantly decreases, whereas our method maintains a high success rate. We find that Wahba's method, when the environment is dense, is likely to fall into a dynamically infeasible local optimum, resulting in unsuccessful trajectories. A comparison of the successful trajectories in the medium-density environment generated by both methods is shown in Fig. 6. Compared to Wahba's method, our method can generate shorter trajectories, especially in the dense environment, which relies on the agility provided by the spatio-temporal deformation of $\mathcal{C}_{\text{MINCO}}$. Besides, there exist obvious abrupt turning points in those trajectories generated by Wahba's method, whereas our trajectories are smoother.

The second experiment tests the responsiveness of the two methods when the MARTS contains different numbers of aerial robots. This experiment is conducted in the medium-density environment. For both planning methods, the numbers of decision variables and constraints scale linearly with the

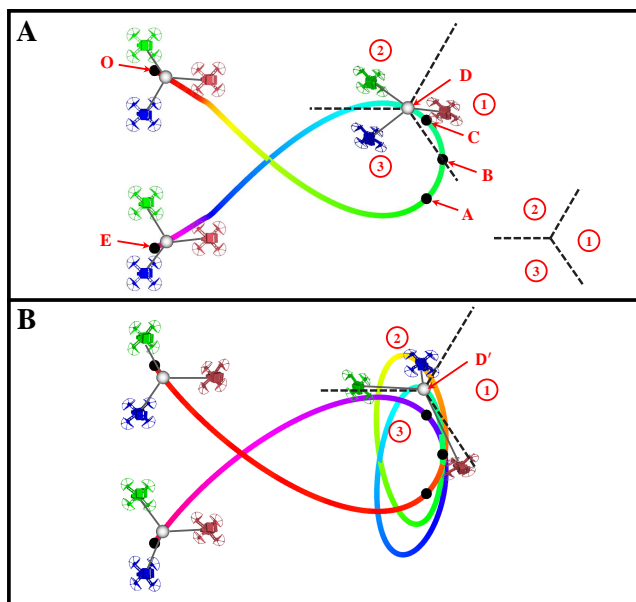


Fig. 8. Ablation study for the cable’s vectorial constraints defined in Eq. 50. The trajectories optimized with and without these constraints are shown in (A) and (B) respectively.

number of aerial robots. Nevertheless, our method reduces the time consumption of trajectory optimization by two orders of magnitude compared to Wahba’s method, and the curve of the time consumption for trajectory optimization as the number of aerial robots grows is shown in Fig. 7. Theoretically, the time consumption of Wahba’s method grows cubically, whereas our planner grows approximately linearly. The reason for the responsiveness improved by our planner is that in each iteration of optimization, as the number of aerial robots increases, the elapsed time for constraint evaluation and penalty functions calculation grows linearly and the elapsed time for trajectory generation ($\varpi^*, \tau^* \rightarrow \mathbf{c}, \mathbf{T}$ as shown in Fig. 2) hardly increases.

B. Ablation Study

The cable’s vectorial constraints defined in Eq. 50 separately restrict the aerial robots as well as their attached cables to three regions, as shown in the lower right corner of Fig. 8A. In this experiment, point O and point E are set as the start and target points of the payload’s trajectory respectively. A, B, and C are fixed waypoints that the payload’s trajectory must pass through. The proposed planning scheme with vectorial constraints optimizes the optimal trajectory with a simple topology, as shown in Fig. 8A, whereas the proposed planning scheme without vectorial constraints falls into a local optimum and generates a trajectory with a complex topology, as shown in Fig. 8B. A major difference between these two trajectories is that at point D’ in Fig. 8B, the relative arrangement of the red and blue aerial robots differs from the initial relative arrangement at the start point O and the final relative arrangement at the target point E, in contrast to the point D in Fig. 8A, where the three aerial robots always maintain a relative arrangement as same as those at the start point O and the target point E.

The main reason for the occurrence of the local optimum in Fig. 8B is that there are infinitely many possible combinations of cables’ force vectors that allow the trajectories to satisfy the payload’s dynamics (Eq. 1b). The planner reduces \mathcal{J}_d , namely the violation of payload’s dynamics too quickly by drastically deforming the aerial robots’ trajectories to an undesirable combination of cables’ force vectors at the expense of the trajectories’ energy \mathcal{J}_E , which leads to an equilibrium between \mathcal{J}_d and \mathcal{J}_E . At this moment, if the planner further optimizes to reduce \mathcal{J}_E , it will inevitably lead to an increase of \mathcal{J}_E , thus inducing this local optimum. Therefore, the vectorial constraints restrict the magnitude of the trajectory deformation by reducing the number of possible combinations among the cables’ force vectors, which greatly alleviates the local optimum.

VIII. REAL WORLD EXPERIMENTS

A. System Configuration

To carry out the real experiments, we deploy a practical MARTS consisting of three aerial robots, each weighing 320g with a wheelbase of 140mm, as shown in Fig. 10. Each aerial robot is equipped with an NVIDIA Jetson Orin NX as the onboard computer, a Kakute H7 MINI as the flight control unit, and a WIFI module. APM firmware is flashed into the flight control unit to get the motor’s speed. An EKF fusing the information from the motion capture system and the IMU is used to estimate the odometry for each aerial robot. The IMU frequency is set to 333Hz. The software modules, including odometry estimation and flight control (both the outer-loop controller and inner-loop controller) run in real-time at IMU’s frequency on the NX computer. The optimized trajectory can be transmitted to each aerial robot through a broadcast network. For the experiments in complex environments, we use FAST-lio2, an excellent LiDAR-inertial odometry framework to get the point cloud data beforehand and then build the ESDF.

B. Control Scheme Validation for Agile Transportation

We validate the performance of our control scheme in the following four aspects. Firstly, the precision of the mass estimation for the payload needs to be evaluated. Secondly, we gradually increase the agility of the trajectory until any aerial robot’s average motor speed approaches the limit to evaluate the tracking error of the control scheme. Thirdly, we test the robustness of the control scheme against common model uncertainties on payload existing in realistic transportation. Finally, we verify whether accurate estimation and compensation for the cable’s force is necessary. We construct four test scenarios and the details are as follows.

1) *Scenario 1. Estimation for Payload’s Mass:* The precise mass of the payload is always not known beforehand. In this experiment, we select five payloads with different masses. The MARTS lifts the payload off the ground and then stabilizes each aerial robot to a predefined hovering position. We estimate each payload’s mass 10 times using Eq. 74 in Sec. VI-C and the results are listed in Fig. 11. All the estimation errors are no more than 8%. In our work, we use a fixed thrust

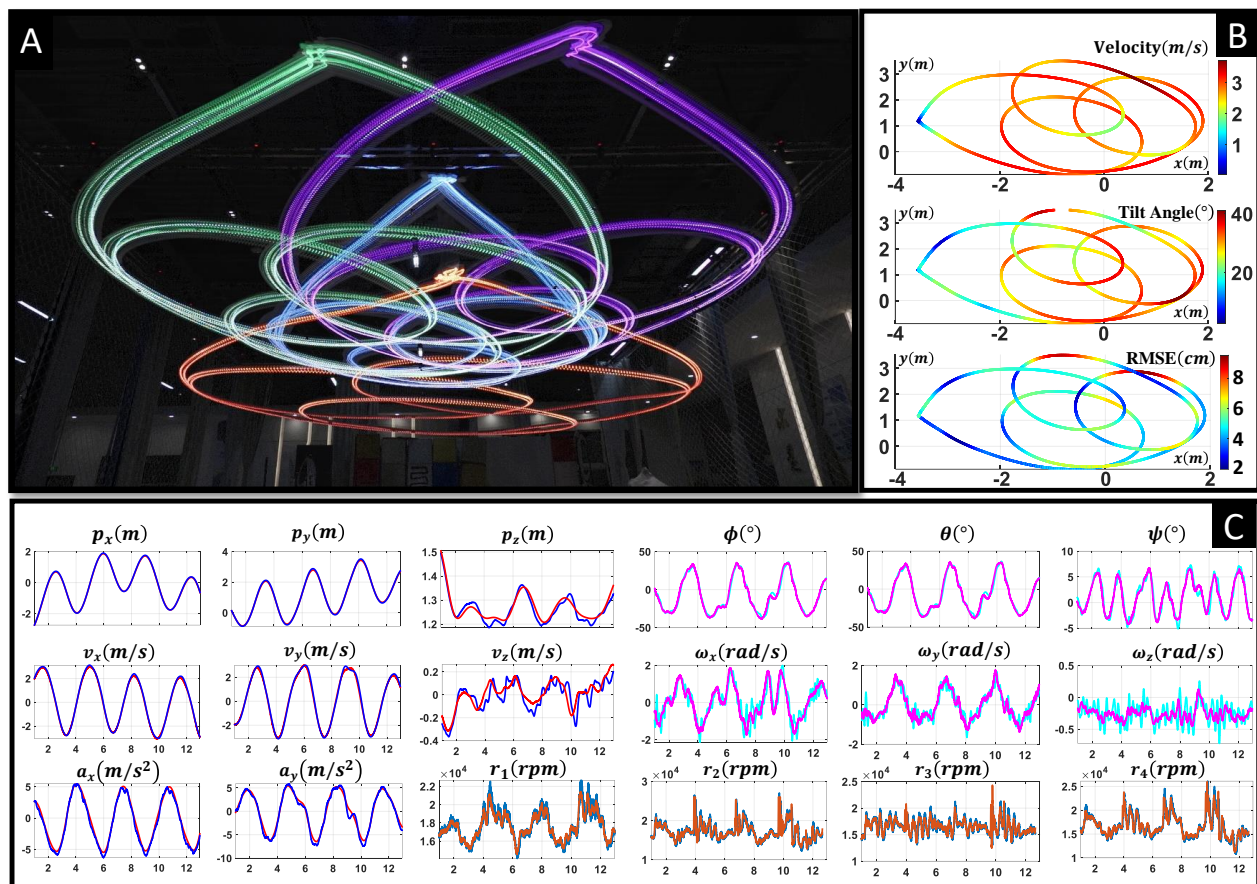


Fig. 9. Control results for tracking agile trajectory in free space, whose agility approaches the limit that the MARTS can successfully execute. (A) Sequential snapshots of the agile transportation trajectory, in which the red curve represents the payload's trajectory and the other three curves represent the three aerial robot's trajectories. (B) The instantaneous velocity, tilt angle, and RMSE of the 2th aerial robot are displayed on its trajectory respectively. (C) The result of trajectory tracking, including the position, velocity, acceleration, attitude, bodyrate, and rotors' RPMs. The curves using colors \square , \square , and \square represent the desired states, and the curves using colors \square , \square , and \square represent the actual state.

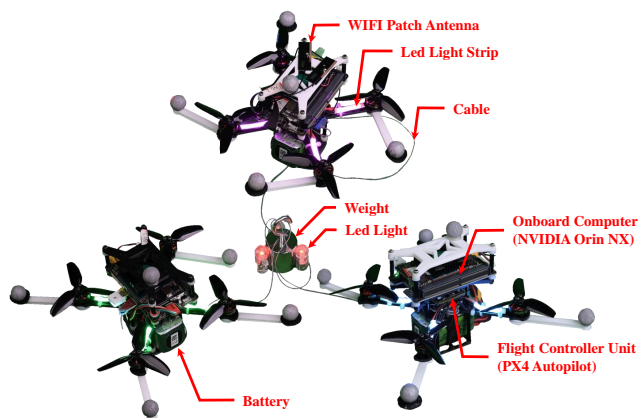


Fig. 10. Illustration of our MARTS consisting of three aerial robots.

coefficient to estimate the actual thrust of the aerial robot, which leads to an estimation error of the actual thrust at different RPMs. The estimation error of the actual thrust, the measurement error of the RPM, and the payload's residual acceleration in z_T -axis while hovering are the main causes of errors in estimating the payload's mass. The results of this

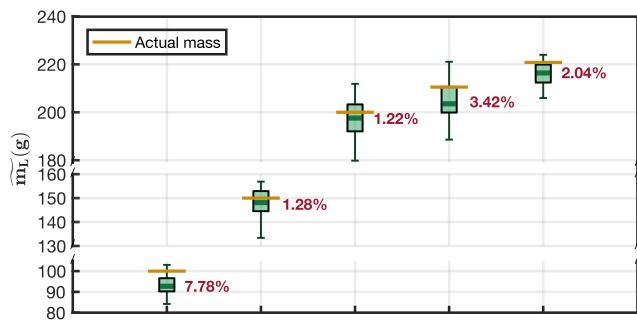


Fig. 11. Estimations for the masses of five different payloads.

experiment show that our method can approximately estimate the mass of the payload.

2) *Scenario 2. Agile Transportation to the Limit of Aerial Robot's Thrust:* Then, we need to validate whether the proposed control scheme can hold the maximum agility of MARTS. For the MARTS, its maximum agility mainly relates to the maximum executable acceleration of the payload. Therefore, we generate a type of agile trajectory as shown in Fig. 9A. Before entering the small circle along the trajectory,

the MARTS needs to be accelerated to a necessary speed to produce a large centripetal acceleration. The increase of the circle's acceleration can be regulated by reducing the duration of the trajectory. Three weights weighing $100g$, $150g$, and $200g$ respectively act as the payload. For each weight, we improve the acceleration of the trajectory as much as possible empirically until the maximum instantaneous average motor's RPM of any aerial robot in the MARTS along the trajectory approaches $24000RPM$ (only $13600RPM$ is required for hovering without a payload). Higher RPM can cause a dramatic drop in battery voltage, leading to system crashes. The maximum velocity (MAX Vel) and maximum acceleration (Max Acc) of the planned trajectory are recorded in Tab. IV. Each trajectory is repeatedly executed 5 times to calculate the root-mean-square error (RMSE) of trajectory tracking. The results indicate that our control scheme can successfully track the agile trajectory up to the limit of thrust that can be provided by the practical aerial robot in the MARTS. Besides, for the MARTS, its allowable agility decreases as the payload's mass increases.

3) *Scenario 3. Comparative Study of Cable's Force Compensation:* In this experiment, we evaluate the effect of accurate force estimation and compensation in outer-loop control of each aerial robot on control error. We replace the accurate force compensation based on INDI in the outer-loop control of the proposed control scheme with the reference force provided by the trajectory as a comparative control scheme. Four trajectories with different maximum velocities are planned for this comparative study. Then we transport a weight weighing $100g$ along each trajectory 5 times using both the control schemes for a comparison. For each trajectory, each control scheme's maximum error (MAXE) along the trajectory and the RMSE are given in Tab. V. We find that both the RMSE and MAXE of the control scheme using reference force are larger than the proposed control scheme. The control scheme using reference force cannot even successfully execute the trajectory with a maximum acceleration of $9.1m/s^2$. For the control scheme using reference force, the inevitable tracking error of payload induces the actual cable's force to periodically deviate from the reference force, leading to oscillation in the positions of aerial robots. This oscillation in turn further worsens the tracking precision of the payload. However, the proposed control scheme can effectively avoid this oscillation since it accurately compensates the actual cable's force. Therefore, this experiment validates the importance of the accurate force

TABLE IV
MAXIMUM AGILITY TESTS OF THE MARTS FOR MULTIPLE WEIGHTS

100g	Max Vel(m/s)	4.4	4.5	4.55	4.6
	Max Acc(m/s^2)	9.104	9.126	9.175	9.184
	RMSE(cm)	4.634	4.916	5.261	6.406
150g	Max Vel(m/s)	4.0	4.1	4.15	4.2
	Max Acc(m/s^2)	7.278	7.859	7.942	8.443
	RMSE(cm)	4.412	4.569	5.454	6.209
200g	Max Vel(m/s)	3.6	3.7	3.75	3.8
	Max Acc(m/s^2)	5.749	6.126	6.292	6.458
	RMSE(cm)	4.553	5.042	5.288	5.574

TABLE V
ABLATION STUDY OF THE FORCE COMPENSATION

Max Acc (m/s^2)	INDI		Reference Force	
	RMSE (cm)	MAXE (cm)	RMSE (cm)	MAXE (cm)
4.9	3.910	7.141	7.898	11.713
6.3	4.129	7.449	8.214	14.667
7.7	4.383	9.315	8.435	17.399
9.1	4.674	10.267	X	X

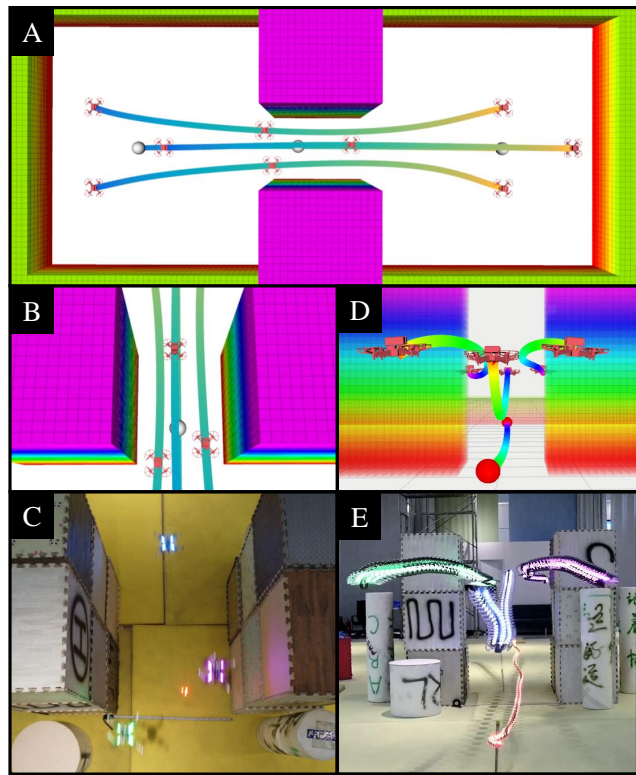


Fig. 12. Illustration of the MARTS passing through a narrow gap. (A) A simulation shows the whole optimized trajectory for safely passing through the gap by regulating the relative position among the aerial robots. (B) A top-view in rviz at the moment of passing through the gap. (C) The snapshot of experiment w.r.t (B). (D) The side-view of the optimized trajectory in rviz. (E) The sequential snapshots of experiment w.r.t (D).

compensation based on INDI to substitute the reference force from the trajectory in the proposed control scheme for agile transportation.

4) *Scenario 4. Robustness Against Payload's Uncertainties:* Since there always exists an uncertainty in the estimation of the payload's mass and an uncertainty induced by the unavoidable swing around the cables' attaching point, we test the robustness of the proposed control scheme against these uncertainties. In this experiment, we use a weight, an express carton, and a water bottle respectively as the payload, all of which weigh $200g$. First, we use $200g$ as the payload's mass to plan a trajectory, which is denoted by $\pm 0\%$. Then, we increase and decrease $200g$ by 10% , 20% , and 30% as the payload's masses for the trajectory planning to simulate the imprecise estimations for the payload's mass and plan six trajectories. We adjust the optimization parameters to ensure the maximum

TABLE VI
RMSES OF MULTIPLE PAYLOADS WITH UNCERTAINTIES

	$\pm 0\%$	+10% -10%	+20% -20%	+30% -30%
Weight	4.472	4.563 4.804	4.747 4.867	4.897 ($\uparrow 9.5\%$) 5.158 ($\uparrow 15.3\%$)
Carton	4.935 ($\uparrow 10.4\%$)	5.243 5.054	5.424 5.142	5.493 ($\uparrow 22.8\%$) 5.450 ($\uparrow 21.9\%$)
Bottle	5.039 ($\uparrow 12.7\%$)	5.227 5.132	5.386 5.383	5.575 ($\uparrow 24.7\%$) 5.499 ($\uparrow 23.0\%$)

velocities of all these 7 trajectories are $3.5m/s$. Each payload tracks each trajectory 5 times to calculate the RMSE. For all these tests, the cable cannot be attached to the payload's CoM strictly and all the payloads are not mass points, which implies that there exists an unavoidable swing of the payload around the attaching point. The RMSEs of these tests are recorded in Tab. VI. From the first column, the RMSEs of the water bottle and the carton are greater than the RMSE of the weight, which shows the detrimental effect of the unavoidable swing induced by the non-mass point payload on the control precision. Besides, for all three payloads, the RMSEs increase with the estimation errors of the payload's mass. Nevertheless, all the payloads can be successfully transported by our MARTS using all these trajectories planned by the imprecise payload's masses, which validate the robustness of the proposed control scheme against the uncertainties on the payload.

C. System Scheme Validation in Various Scenarios

We further construct a variety of scenarios to validate the performance of our MARTS, including the safety of agile transportation in complex environments, the agility of trajectory in narrow spaces, and the responsiveness of trajectory planning. The details are described as follows.

1) *Continuous S-shaped Turns*: An experimental environment with multiple consecutive S-shaped turns is constructed as shown in Fig. 1B. In this experiment, a safe and agile trajectory of $24.43m$ is planned just using $162ms$. The MARTS transports a payload of $200g$ smoothly through these consecutive S-shaped turns and reaches the target point, without colliding with any obstacle. This experiment validates the capability of our planning scheme to generate a safe and agile trajectory in real time.

2) *Narrow Gap*: We construct a narrow gap with a width of $1m$ smaller than the initial size ($1.6m$) of the MARTS. In this experiment, our planning scheme contracts the lateral size of the MARTS by optimizing all the cables' directions to ensure safe transportation through the narrow gap. As shown in Fig. 12, the result validates that our planning scheme can generate an agile trajectory by adjusting the configuration of MARTS to ensure the system's safety, which enhances its adaptability to narrow spaces. This experiment verifies the agility of the trajectory planned by our planning scheme.

3) *Emergent Replanning Towards a New Target*: In many missions, the responsiveness of replanning is important for mission efficiency. To validate the responsiveness of our planning scheme, we artificially construct an emergent replanning

scenario as shown in Fig. 13A. This test consists of the following five phases. 1. The trajectory \overline{OE} is generated after the point E is selected as the target. 2. The MARTS flies along the trajectory \overline{OE} , and we select a new target point F for the MARTS when the payload reaches point A . 3. The planning module takes the state at point C , which is $100ms$ ahead of point A , as the initial state and replans the trajectory. 4. The MARTS continually flies along the trajectory \overline{AE} until it receive a new trajectory \overline{CF} at the point B . 5. At point C , the MARTS switches the trajectory from trajectory \overline{OE} to \overline{CF} . Thanks to the real-time capability, our planning module just uses $72ms$ to replan a new trajectory, which depresses the elapsed time required for replanning and thus strives for a larger safe distance away from the obstacle. Besides, an agile trajectory is generated by our planning scheme so that the MARTS can bypass the obstacle using a large maneuver and successfully switch the trajectory topology within this limited safe distance, which further improves the efficiency of MARTS. Fig. 13C-D are the snapshots of this maneuver.

4) *Consecutively Replanning*: Finally, to further validate the responsiveness of our planning scheme for replanning, we serially select the target A , B , C , and D around the obstacle for the MARTS to construct a consecutively replanning scenario, as shown in Fig. 14. All the replannings are carried out within $50ms \sim 80ms$ and continuous state transitions are guaranteed for smooth trajectory switching at points A' , B' , and C' . The result of this experiment, as well as the result of the previous experiment sufficiently verify the responsiveness of our planning scheme. For more details, please watch the experimental video.

IX. CONCLUSION

In this paper, we carefully derive the flatness maps for the aerial robot in the MARTS subject to dynamics coupling with payload and kinematic constraints provided by cable. A real-time trajectory planning scheme is proposed to generate safe, dynamically feasible, and agile trajectories for the MARTS in complex environments. A robust and distributed control scheme is proposed to track agile trajectory without relying on the closed-loop control and state measurement for both the payload and cable, even if there exists uncertainty on the payload. Finally, we deploy a practical MARTS containing three aerial robots with adequate simulations and experiments to validate the effectiveness of our planner and control schemes and exhibit great application value.

REFERENCES

- [1] K. Sreenath, T. Lee, and V. Kumar, "Geometric control and differential flatness of a quadrotor uav with a cable-suspended load," in *52nd IEEE conference on decision and control*. IEEE, 2013, pp. 2269–2274.
- [2] P. Foehn, D. Falanga, N. Kuppuswamy, R. Tedrake, and D. Scaramuzza, "Fast trajectory optimization for agile quadrotor maneuvers with a cable-suspended payload," July 2017.
- [3] S. Tang, V. Wüest, and V. Kumar, "Aggressive flight with suspended payloads using vision-based control," *IEEE Robotics and Automation Letters*, vol. 3, no. 2, pp. 1152–1159, 2018.
- [4] C. Y. Son, H. Seo, D. Jang, and H. J. Kim, "Real-time optimal trajectory generation and control of a multi-rotor with a suspended load for obstacle avoidance," *IEEE Robotics and Automation Letters*, vol. 5, no. 2, pp. 1915–1922, 2020.

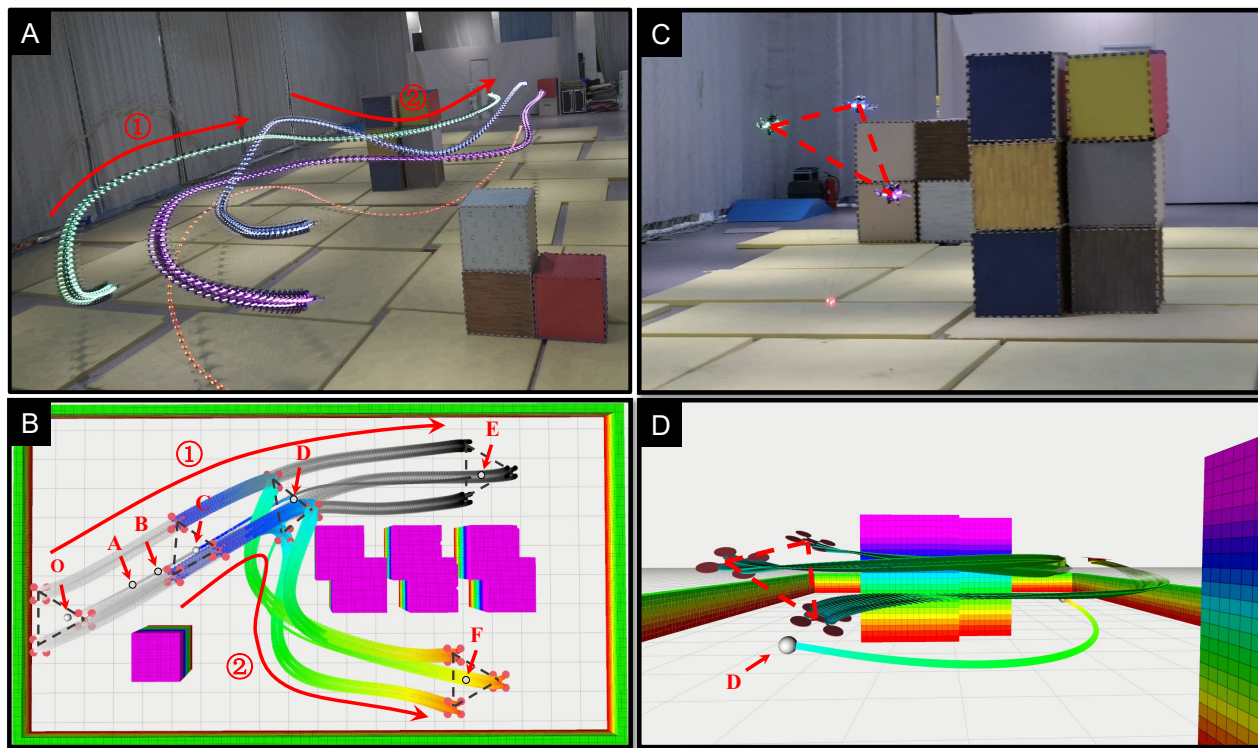


Fig. 13. Illustration of an emergent replanning for the MARTS towards a new target. (A) Actual experiment and the trajectories of the MARTS. (B) The simulation schematic for this emergency replanning. (C) Special zoomed-in view of the MARTS for the frame at point D. (D) The side-view of the simulation schematic for this emergency replanning.

- [5] J. Zeng, P. Kotaru, M. W. Mueller, and K. Sreenath, "Differential flatness based path planning with direct collocation on hybrid modes for a quadrotor with a cable-suspended payload," *IEEE Robotics and Automation Letters*, vol. 5, no. 2, pp. 3074–3081, 2020.
- [6] S. Belkhale, R. Li, G. Kahn, R. McAllister, R. Calandra, and S. Levine, "Model-based meta-reinforcement learning for flight with suspended payloads," *IEEE Robotics and Automation Letters*, vol. 6, no. 2, pp. 1471–1478, 2021.
- [7] G. Yu, D. Cabecinhas, R. Cunha, and C. Silvestre, "Aggressive maneuvers for a quadrotor-slung-load system through fast trajectory generation and tracking," *Autonomous Robots*, vol. 46, no. 4, pp. 499–513, 2022.
- [8] H. Li, H. Wang, C. Feng, F. Gao, B. Zhou, and S. Shen, "Autotrans: A complete planning and control framework for autonomous uav payload transportation," *IEEE Robotics and Automation Letters*, vol. 8, no. 10, pp. 6859–6866, 2023.
- [9] H. Wang, H. Li, B. Zhou, F. Gao, and S. Shen, "Impact-aware planning and control for aerial robots with suspended payloads," *IEEE Transactions on Robotics*, vol. 40, pp. 2478–2497, 2024.
- [10] D. Mellinger, M. Shomin, N. Michael, and V. Kumar, "Cooperative grasping and transport using multiple quadrotors," in *Distributed Autonomous Robotic Systems: The 10th International Symposium*. Springer, 2013, pp. 545–558.
- [11] G. Loianno and V. Kumar, "Cooperative transportation using small quadrotors using monocular vision and inertial sensing," *IEEE Robotics and Automation Letters*, vol. 3, no. 2, pp. 680–687, 2017.
- [12] Z. Wang, S. Singh, M. Pavone, and M. Schwager, "Cooperative object transport in 3d with multiple quadrotors using no peer communication," in *2018 IEEE International Conference on Robotics and Automation (ICRA)*. IEEE, 2018, pp. 1064–1071.
- [13] M. Bernard, K. Kondak, I. Maza, and A. Ollero, "Autonomous transportation and deployment with aerial robots for search and rescue missions," *Journal of Field Robotics*, vol. 28, no. 6, pp. 914–931, 2011.
- [14] C. Masone, H. H. Bühlhoff, and P. Stegagno, "Cooperative transportation of a payload using quadrotors: A reconfigurable cable-driven parallel robot," in *2016 IEEE/RSJ International Conference on Intelligent Robots and Systems (IROS)*. IEEE, 2016, pp. 1623–1630.
- [15] P. Prajapati, S. Parekh, and V. Vashista, "On the human control of a multiple quadcopters with a cable-suspended payload system," in *2020 IEEE international conference on robotics and automation (ICRA)*. IEEE, 2020, pp. 2253–2258.
- [16] G. Li, X. Liu, and G. Loianno, "Rotortm: A flexible simulator for aerial transportation and manipulation," *IEEE Transactions on Robotics*, vol. 40, pp. 831–850, 2024.
- [17] E. Kaufmann, L. Bauersfeld, A. Loquercio, M. Müller, V. Koltun, and D. Scaramuzza, "Champion-level drone racing using deep reinforcement learning," *Nature*, vol. 620, no. 7976, pp. 982–987, 2023.
- [18] N. Michael, J. Fink, and V. Kumar, "Cooperative manipulation and transportation with aerial robots," *Autonomous Robots*, vol. 30, pp. 73–86, 2011.
- [19] J. Fink, N. Michael, S. Kim, and V. Kumar, "Planning and control for cooperative manipulation and transportation with aerial robots," *The International Journal of Robotics Research*, vol. 30, no. 3, pp. 324–334, 2011.
- [20] Q. Jiang and V. Kumar, "The inverse kinematics of cooperative transport with multiple aerial robots," *IEEE Transactions on Robotics*, vol. 29, no. 1, pp. 136–145, 2012.
- [21] M. Manubens, D. Devaurs, L. Ros, and J. Cortés, "Motion planning for 6-d manipulation with aerial towed-cable systems," in *Proceedings of Robotics: Science and Systems*, Berlin, Germany, June 2013, p. 8p.
- [22] K. Sreenath and V. Kumar, "Dynamics, control and planning for cooperative manipulation of payloads suspended by cables from multiple quadrotor robots," June 2013.
- [23] D. Mellinger and V. Kumar, "Minimum snap trajectory generation and control for quadrotors," in *2011 IEEE international conference on robotics and automation*. IEEE, 2011, pp. 2520–2525.
- [24] B. E. Jackson, T. A. Howell, K. Shah, M. Schwager, and Z. Manchester, "Scalable cooperative transport of cable-suspended loads with uavs using distributed trajectory optimization," *IEEE Robotics and Automation Letters*, vol. 5, no. 2, pp. 3368–3374, 2020.
- [25] S. Sun and A. Franchi, "Nonlinear mpc for full-pose manipulation of a cable-suspended load using multiple uavs," in *2023 International Conference on Unmanned Aircraft Systems (ICUAS)*. IEEE, 2023, pp. 969–975.
- [26] K. Wahba, J. Ortiz-Haro, M. Toussaint, and W. Hönig, "Kinodynamic motion planning for a team of multirotors transporting a cable-suspended payload in cluttered environments," *arXiv preprint arXiv:2310.03394*, 2023.

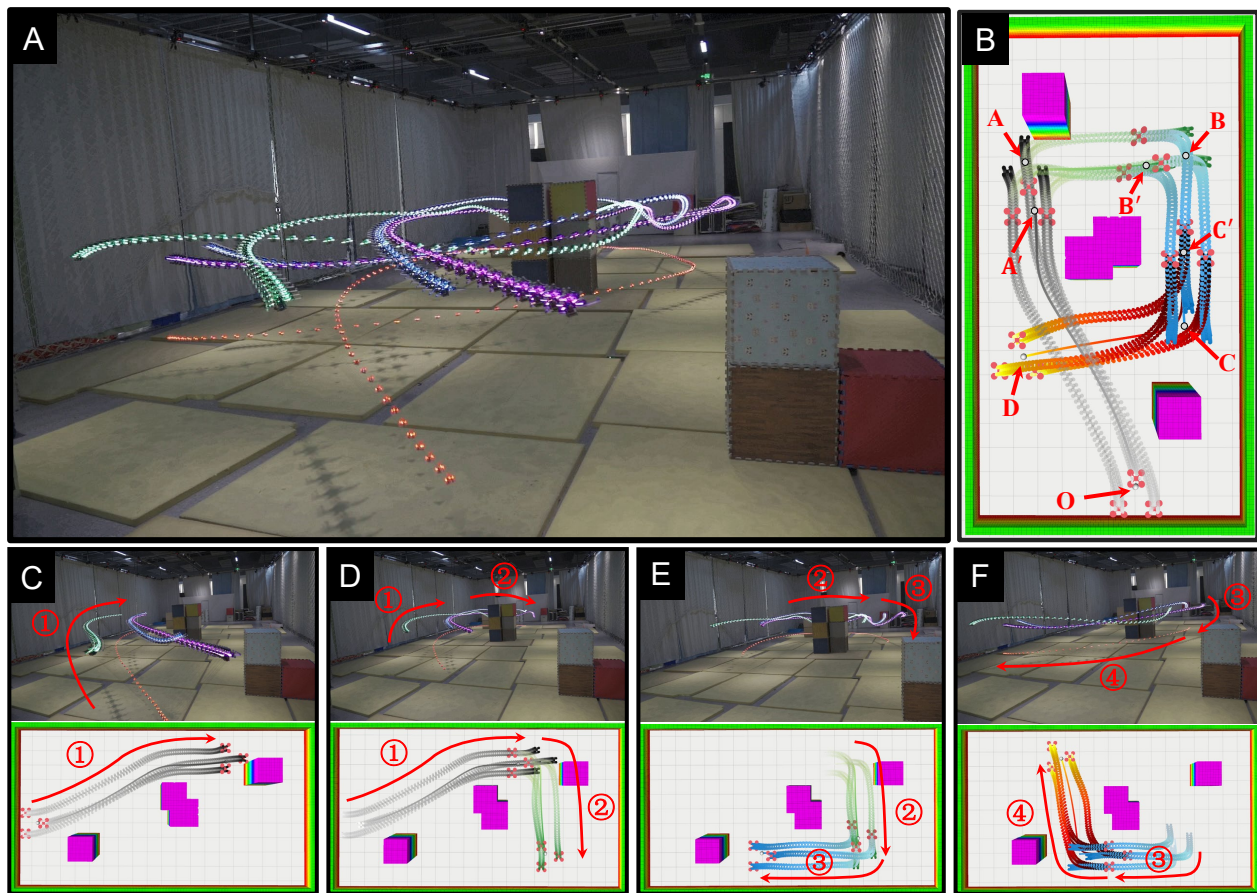


Fig. 14. Illustration of consecutively replanning for the MARTS towards new targets. (A) Sequential snapshot of the MARTS in the experiment. (B) Simulation schematic for consecutively replanning. (C) The planned trajectory \overline{OA} for the first target point A. (D) The replanned trajectory $\overline{A'B}$ for the second target point B. (E) The replanned trajectory $\overline{B'C}$ for the third target point C. (F) The replanned trajectory $\overline{C'D}$ for the fourth target point D.

- [27] T. Lee, K. Sreenath, and V. Kumar, "Geometric control of cooperating multiple quadrotor uavs with a suspended payload," in *52nd IEEE conference on decision and control*. IEEE, 2013, pp. 5510–5515.
- [28] T. Lee, "Geometric control of quadrotor uavs transporting a cable-suspended rigid body," *IEEE Transactions on Control Systems Technology*, vol. 26, no. 1, pp. 255–264, 2017.
- [29] G. Li, R. Ge, and G. Loianno, "Cooperative transportation of cable suspended payloads with mavs using monocular vision and inertial sensing," *IEEE Robotics and Automation Letters*, vol. 6, no. 3, pp. 5316–5323, 2021.
- [30] J. Geng and J. W. Langelaan, "Cooperative transport of a slung load using load-leading control," *Journal of Guidance, Control, and Dynamics*, vol. 43, no. 7, pp. 1313–1331, 2020.
- [31] G. Li and G. Loianno, "Nonlinear model predictive control for cooperative transportation and manipulation of cable suspended payloads with multiple quadrotors," in *2023 IEEE/RSJ International Conference on Intelligent Robots and Systems (IROS)*. IEEE, 2023, pp. 5034–5041.
- [32] K. Wahba and W. Hönig, "Efficient optimization-based cable force allocation for geometric control of a multirotor team transporting a payload," *IEEE Robotics and Automation Letters*, vol. 9, no. 4, pp. 3688–3695, 2024.
- [33] K. Klausen, C. Meissen, T. I. Fossen, M. Arcaç, and T. A. Johansen, "Cooperative control for multirotors transporting an unknown suspended load under environmental disturbances," *IEEE Transactions on Control Systems Technology*, vol. 28, no. 2, pp. 653–660, 2018.
- [34] H. G. De Marina and E. Smeur, "Flexible collaborative transportation by a team of rotorcraft," in *2019 International Conference on Robotics and Automation (ICRA)*. IEEE, 2019, pp. 1074–1080.
- [35] M. Gassner, T. Cieslewski, and D. Scaramuzza, "Dynamic collaboration without communication: Vision-based cable-suspended load transport with two quadrotors," in *2017 IEEE International Conference on Robotics and Automation (ICRA)*. IEEE, 2017, pp. 5196–5202.
- [36] M. Tognon, C. Gabellieri, L. Pallottino, and A. Franchi, "Aerial co-manipulation with cables: The role of internal force for equilibria, stability, and passivity," *IEEE Robotics and Automation Letters*, vol. 3, no. 3, pp. 2577–2583, 2018.
- [37] A. Tagliabue, M. Kamel, R. Siegwart, and J. Nieto, "Robust collaborative object transportation using multiple mavs," *The International Journal of Robotics Research*, vol. 38, no. 9, pp. 1020–1044, 2019.
- [38] W. Xu, Y. Cai, D. He, J. Lin, and F. Zhang, "Fast-lio2: Fast direct lidar-inertial odometry," *IEEE Transactions on Robotics*, vol. 38, no. 4, pp. 2053–2073, 2022.
- [39] E. Tal and S. Karaman, "Accurate tracking of aggressive quadrotor trajectories using incremental nonlinear dynamic inversion and differential flatness," *IEEE Transactions on Control Systems Technology*, vol. 29, no. 3, pp. 1203–1218, 2021.
- [40] M. Watterson and V. Kumar, "Control of quadrotors using the hopf fibration on $so(3)$," in *Robotics Research: The 18th International Symposium ISRR*. Springer, 2019, pp. 199–215.
- [41] Z. Wang, X. Zhou, C. Xu, and F. Gao, "Geometrically constrained trajectory optimization for multirotors," *IEEE Transactions on Robotics*, vol. 38, no. 5, pp. 3259–3278, 2022.
- [42] L. S. Jennings and K. L. Teo, "A computational algorithm for functional inequality constrained optimization problems," *Automatica*, vol. 26, no. 2, pp. 371–375, 1990.
- [43] W. H. Press, S. A. Teukolsky, W. T. Vetterling, and B. P. Flannery, *Numerical Recipes 3rd Edition: The Art of Scientific Computing*, 3rd ed. USA: Cambridge University Press, 2007.
- [44] J. Pan, S. Chitta, and D. Manocha, "Fcl: A general purpose library for collision and proximity queries," in *2012 IEEE International Conference on Robotics and Automation*. IEEE, 2012, pp. 3859–3866.
- [45] J. Ortiz-Haro, W. Hönig, V. N. Hartmann, and M. Toussaint, "idb-a*: Iterative search and optimization for optimal kinodynamic motion planning," *IEEE Transactions on Robotics*, pp. 1–19, 2024.

- [46] C. Mastalli, R. Budhiraja, W. Merkt, G. Saurel, B. Hammoud, M. Naveau, J. Carpentier, L. Righetti, S. Vijayakumar, and N. Mansard, "Crocoddyl: An efficient and versatile framework for multi-contact optimal control," in *2020 IEEE International Conference on Robotics and Automation (ICRA)*. IEEE, 2020, pp. 2536–2542.